2007-09

MEMS polymumps-based miniature microphone for directional sound sensing

Shivok, Timothy J.

Monterey, California. Naval Postgraduate School

NAVAL POSTGRADUATE SCHOOL

MONTEREY, CALIFORNIA

THESIS

MEMS POLYMUMPS-BASED MINIATURE MICROPHONE FOR DIRECTIONAL SOUND SENSING

by

Timothy J. Shivok

September 2007

Thesis Advisor:	Gamani Karunasiri
Co-Advisor:	Jose O. Sinibaldi

Approved for public release; distribution is unlimited

THIS PAGE INTENTIONALLY LEFT BLANK

REPORT DOCUMENTATION PAGE		Form Approved OMB No. 0704-0188

1. AGENCY USE ONLY *(Leave blank)*	2. REPORT DATE September 2007	3. REPORT TYPE AND DATES COVERED Master's Thesis

4. TITLE AND SUBTITLE MEMS PolyMUMPS-Based Miniature Microphone for Directional Sound Sensing	5. FUNDING NUMBERS
6. AUTHOR(S) Timothy J. Shivok	
7. PERFORMING ORGANIZATION NAME(S) AND ADDRESS(ES) Naval Postgraduate School Monterey, CA 93943-5000	8. PERFORMING ORGANIZATION REPORT NUMBER
9. SPONSORING /MONITORING AGENCY NAME(S) AND ADDRESS(ES) N/A	10. SPONSORING/MONITORING AGENCY REPORT NUMBER

11. SUPPLEMENTARY NOTES The views expressed in this thesis are those of the author and do not reflect the official policy or position of the Department of Defense or the U.S. Government.

12a. DISTRIBUTION / AVAILABILITY STATEMENT Approved for public release; distribution unlimited	12b. DISTRIBUTION CODE

13. ABSTRACT (maximum 200 words)

A miniature directional sound sensor was fabricated using micro-electro-mechanical system (MEMS) technology based on the operational principle of Ormia ochracea fly's hearing organ. The fly uses coupled bars hinged at the center to achieve the directional sound sensing by monitoring the difference in vibration amplitude between them. The MEMS sensor design employed in this thesis was fabricated using the PolyMUMPs process. The sound sensor has two primary vibrational modes (rocking and bending) which were simulated by finite element analysis and tested by actuating the sensor using both electrostatics and sound. The experimentally observed vibrational frequencies were found to be in good agreement with that of the modeling but the amplitudes of vibration were found to be relatively small compared to the expected values. The design of optimized sensors, with larger amplitude of vibration hence high sensitivity, will be discussed in this presentation.

14. SUBJECT TERMS PolyMUMPs, MEMS, Ormia, Ormia Ochracea, Biomimetic, Directional Microphone, Sensors, Microphone, USW, Fly Hearing, Undersea Warfare	15. NUMBER OF PAGES 106
	16. PRICE CODE

17. SECURITY CLASSIFICATION OF REPORT	18. SECURITY CLASSIFICATION OF THIS PAGE	19. SECURITY CLASSIFICATION OF ABSTRACT	20. LIMITATION OF ABSTRACT
Unclassified	Unclassified	Unclassified	UU

NSN 7540-01-280-5500

Standard Form 298 (Rev. 2-89)
Prescribed by ANSI Std. 239-18

THIS PAGE INTENTIONALLY LEFT BLANK

Approved for public release; distribution unlimited

MEMS POLYMUMPS-BASED MINIATURE MICROPHONE FOR DIRECTIONAL SOUND SENSING

Timothy J. Shivok
Lieutenant, United States Navy
B.S., Thomas Edison State College, 2000

Submitted in partial fulfillment of the
requirements for the degree of

MASTER OF SCIENCE IN APPLIED PHYSICS

from the

NAVAL POSTGRADUATE SCHOOL
September 2007

Author: Timothy J. Shivok

Approved by: Gamani Karunasiri
Thesis Advisor

Jose O. Sinibaldi
Co-Advisor

James H. Luscombe
Chairman, Department of Physics

THIS PAGE INTENTIONALLY LEFT BLANK

ABSTRACT

A miniature directional sound sensor was fabricated using micro-electro-mechanical system (MEMS) technology based on the operational principle of Ormia ochracea fly's hearing organ. The fly uses coupled bars hinged at the center to achieve the directional sound sensing by monitoring the difference in vibration amplitude between them. The MEMS sensor design employed in this thesis was fabricated using the PolyMUMPs process. The sound sensor has two primary vibrational modes (rocking and bending) which were simulated by finite element analysis and tested by actuating the sensor using both electrostatics and sound. The experimentally observed vibrational frequencies were found to be in good agreement with that of the modeling but the amplitudes of vibration were found to be relatively small compared to the expected values. The design of optimized sensors, with larger amplitude of vibration hence high sensitivity, will be discussed in this presentation.

THIS PAGE INTENTIONALLY LEFT BLANK

TABLE OF CONTENTS

I. INTRODUCTION 1
A. BACKGROUND 2
1. Biological Motivation 2
a. Fly's Auditory Mechanics 3
b. Simplified Mechanical System 4
B. PHYSICS OF WORKING SYSTEM 5
1. Simple Two Degrees of Freedom Spring-Mass-Damper System 5
2. Fly's Mechanical Model 9
3. Eigen Frequency Modes 11
a. Rocking Mode and Bending Modes 12
4. Displacement due to Sound 12
5. Determination of the Direction of Sound 17
a. Sensed Time Difference 17
C. MATLAB PROGRAM TO VISUALIZE SYSTEM WORKING 18
1. Sound from Zero Degrees 19
2. Sound from 30 Degrees 20
3. Sound from 60 Degrees 22

II. BIOMIMETIC MEMS DESIGN 23
A. MERITS OF THE POLYMUMPS PROCESS 23
1. PolyMUMPs Process Definition 24
B. BIOMIMETIC MEMS DESIGN 26
1. The Primary Design 29
a. Reasons for Additional Components 30
b. 3D View of Primary Device (without Electrodes) 32
C. CHIP LAYOUT 32

III. *COMSOL* MODE SIMULATION 35
A. *COMSOL* MODE SIMULATION PROCESS 35
1. Rocking and Bending Modes 38
B. COMPARISON OF *ANSYS* AND *COMSOL* SIMULATION RESULTS 40

IV. DEVICE TESTING 43
A. WIRING AND PACKAGING 43
B. EXPERIMENTAL SETUP 47
1. Functions of Equipment Used 47
C. ELECTROSTATIC TESTING 48
1. Visual Results 51
2. Computer Controlled Evaluation Board with M3110 Capacitance Measurement Chip 53
D. SOUND TESTING 54

1. Polytec Laser Vibrometer 55
2. Results 55
E. ADDITIONAL INFORMATION OBTAINED FROM FREQUENCY RESPONSE CURVES 56
V. POSSIBLE REASONS FOR DIFFERENCES BETWEEN SIMULATIONS AND EXPERIMENTAL RESULTS 59
A. TOLERANCES IN STRUCTURE SIZE 59
B. SIMULATION SIMPLIFICATIONS 60
1. Revised *COMSOL* Simulation Results 60
C. HOLE SIZE TOO LARGE CAUSING SOUND LEAKAGE 61
1. Solid Plate Membrane 61
2. Affect of Holes in the Membrane 62
D. INCORPORATION OF SQUEEZE FILM DAMPING INTO THE SIMULATIONS 64
1. *COMSOL* Process 64
2. Device #19 Results 66
VI. CONCLUSION 69
VII. RECOMMENDATIONS FOR FUTURE WORK 71
A. INVESTIGATION OF SOIMUMPS PROCESS 71
B. *COMSOL* SIMULATIONS OF THE SOIMUMPS PROCESS 72
C. ADDITIONAL WORK 72
APPENDIX A – *MATLAB CODE SAMPLE FOR FLY ANIMATION* 75
APPENDIX B – DR. KIM'S *ANSYS* CODE 79
APPENDIX C – PROOF OF $FW\sqrt{2}M$ 85
LIST OF REFERENCES 87
INITIAL DISTRIBUTION LIST 89

LIST OF FIGURES

Figure 1. Fly's auditory system and mechanical components (After: Miles *et al.*, 1995). 4
Figure 2. Simplified mechanical equivalent of the fly's ear system (From: Miles *et al.*, 1995). 5
Figure 3. Two degrees of freedom spring-mass-damper system (After: Rao, 2003). 6
Figure 4. Free-body diagram (After: Rao, 2003). 6
Figure 5. Simplified mechanical equivalent of the fly's hearing System (After: Miles *et al.*, 1995). 9
Figure 6. Fly free-body diagram. 10
Figure 7. Ear vibration Eigen modes (After: Robert *et al.*, 1996). 12
Figure 8. Frequency response of the ears based on the model (From: Karunasiri *et al.,* 2005). 15
Figure 9. Transient response based on the model for 45 degree inclined 5kHz sound wave (After: Karunasiri *et al.,* 2005). 16
Figure 10. Sensed time difference for different frequencies and angles. 18
Figure 11. Zero degrees incidence with bars up. 19
Figure 12. Still zero degrees and the bars moved down. 19
Figure 13. Zero degrees and bars moved completely down. 20
Figure 14. 30 degree incident sound with bars horizontal. 21
Figure 15. 30 degree incident sound with bars up – red bar higher amplitude. 21
Figure 16. 30 degree incident sound with bars down– red bar higher amplitude. 22
Figure 17. 60 degree incident sound with bars down–red bar highest amplitude. 22
Figure 18. PolyMUMPs layering and thicknesses (After: Koester *et al.*, 2003). 25
Figure 19. Schematic diagram of fly ear using MEMS (After: Karunasiri *et al.*, 2005). 26
Figure 20. PolyMUMPs design of directional sensor. 27
Figure 21. Depth view of a typical PolyMUMPs design. 28
Figure 22. Primary PolyMUMPs design. 29
Figure 23. View of primary device electrodes. 30
Figure 24. View of grating structure attached to a wing. 31
Figure 25. Workings of diffraction grating (From: Kim *et al.,* 2005). 31
Figure 26. 3D View of primary device without electrodes. 32
Figure 27. Chip layout. 33
Figure 28. Primary device with fixed boundary conditions. 36
Figure 29. Normally meshed primary device. 37
Figure 30. Solver parameters settings. 38
Figure 31. Time sequence of (a) rocking and (b) bending modes. 39
Figure 32. Primary device in rocking mode representing time 1 in Figure 30 (a). 39

Figure 33. Primary device in bending mode representing time 1 in Figure 30 (b). 40
Figure 34. Optical microscope view of primary device. The wing structure is 1080 micrometers by 1080 micrometers. 43
Figure 35. Chip in its package and wired. 44
Figure 36. Outer devices wiring diagram. 45
Figure 37. Inner devices wiring diagram. 46
Figure 38. Pin numbering diagram. Pins are on the back. Numbered as if seen from the front. Numbers correspond to its same number pad. 46
Figure 39. Equipment in lab setup used for measuring vibrational amplitudes. ... 47
Figure 40. Device 4, magnitude of velocity versus frequency curve. 49
Figure 41. Device 8, magnitude of velocity versus frequency curve. 50
Figure 42. Device 19, magnitude of velocity versus frequency curve. 51
Figure 43. Device 19 electrostatically driven rocking mode. 52
Figure 44. Device 19 electrostatically driven bending mode. 52
Figure 45. Device 19 electrostatically driven, at 4.75 kHz, rocking mode detailed view. 53
Figure 46. Computer controlled evaluation board with M3110 capacitance measurement chip. 54
Figure 47. Actuation of device 19 using sound incident normal to the membrane surface. The bending mode can be clearly seen from the time series. 55
Figure 48. Velocity as a function of excitation frequency for device 19. 57
Figure 49. Device 19 optical microscope view with measurements. 59
Figure 50. Device 19 *COMSOL* simulation with gold layer. 60
Figure 51. Solid Plate, sound actuated 45 degrees left to right, *COMSOL* simulation screen shot. 62
Figure 52. *COMSOL* simulation screen shot of the device 19 under the same sound field as the solid plate in Figure 51. 63
Figure 53. Film damping settings based on Veijola *et al.* 2005 paper (From: Veijola *et al.*, 2005). 65
Figure 54. Film damping settings for the regions defined as holes. 65
Figure 55. Film damping settings for the regions not defined as holes. 66
Figure 56. Device 19 damping pressure results for actuation at 6.1kHz for a one Pascal force. 67
Figure 57. Recommend Sensor layout with perforated holes on the back plate to increase vibration amplitude and reduce squeezed film damping. . 71
Figure 58. Recommend Sensor layout side view showing etched holes under wing structure. Again substrate is 400-500 micrometers thick, while the wings are only 10 micrometers thick, so this is not drawn to scale. 72

LIST OF TABLES

Table 1. Design parameters used for the chip in Figure 27. 33
Table 2. *ANSYS* vs *COMSOL* simulations for the chip in Figure 27. 41
Table 3. Comparison of simulated and experimental displacements 63

THIS PAGE INTENTIONALLY LEFT BLANK

ACKNOWLEDGMENTS

I would like to express my gratitude to:

Professor Gamani Karunasiri for his physics guidance and MEMS expertise throughout this project.

Professor Jose O. Sinibaldi for his mechanical engineering guidance and MEMS expertise throughout this project.

Dr. Byungki Kim for his initial work on this device and his mentoring during turnover of the project to me.

Professor Steve Baker for his acoustics guidance throughout this project.

Professor Arlene Guest for her MATLAB guidance and assistance on the program to visually represent the fly's ears working.

Dr. John Dunec for his guidance and assistance with the finite element multi-physics program, *COMSOL*. This program was used for most of the simulations.

Teledyne Technologies for their support in allowing us to use their laser vibrometer during initial testing phase; specifically Jeffrey DeNatale Manager of their MEMS Department.

SPAWAR (San Diego) for their generous award of the $10,000 Fellowship to work on this Thesis; specifically, Dr. Waters for his mentorship on the project and frequent visits to NPS.

NSF for their generous founding of the project and vote of confidence in the concept.

Jeffrey Catterlin, a high school intern, for his MANY probing questions during his internship. His questions pushed me to understand even more of how this system worked so that I could try to answer ALL of his questions. [Jeff best of luck at UC Irvine in the fall.]

Lastly, I would like to extend a special thanks to my wife, Linda, for her love, support, and patience while I was earning this Master's of Science degree.

I. INTRODUCTION

"Conn, Sonar, possible submerged contact bearing 030 or 290," bellows from the announcing circuit aboard a fast attack submarine. "Helm, right ten degrees rudder", the Officer of the Deck orders as he wonders why someone had not invented a better way of pinpointing which side of the towed array a contact was on. Current towed array technology uses an array of omni-directional hydrophones. Because of this, the towed array inherently has a bearing ambiguity that can only be resolved using the Doppler Effect of sound. Turning the submarine either toward or away from the contact would cause a frequency shift in the received sound and thus indicate which side of the array the contact was on. If frequency went up, then the submarine turned towards, and if frequency went down, it turned away. There are two major problems with this technique however. First it assumes that the contact does not maneuver while the submarine maneuvered, which is not always the case. Secondly, it reduces the submarine's stealth, because as it turns through the water, the submarine itself makes noise. If a directional microphone was developed and perfected it could be added to existing towed arrays, and could eliminate the practice of needing to turn the submarine to resolve bearing ambiguity, thereby improving submarine stealth. Eventually new arrays could be built completely via these microphones.

Unmanned Aerial Vehicles (UAV's) or Unmanned Underwater Vehicles (UUVs) currently cannot autonomously turn to investigate an explosion occurring on its right or left side for further analysis. Existing sensors cannot determine the angle the sound came from in order for the autonomous system to decide which way to turn the vehicle. Unfortunately, an explosion is too short in duration to use the Doppler Effect to determine the bearing to the explosion; so current searches must involve a system with less than full autonomy. This practice could be eliminated if an array of directional microphones, small enough with low power consumption, could be developed and perfected.

If a ground soldier is being fired upon by a sniper, which is hidden in some aspect, then it might be a very good intelligence point if the bearing of the gun fire is known. If a directional microphone was developed and perfected it could determine the bearing and thus a detailed inspection of the area could be conducted, perhaps saving lives.

There are a multitude of places in the military where it might be important to know the bearing of the incident sound. Therefore if a directional microphone was developed and perfected, there are endless applications within the military. Basically, anywhere there is a need to know what direction the sound came from, on a low cost, small scale, and low power consuming aspect this perfected directional microphone is the military's solution.

A. BACKGROUND

As is often the case, biology has solved the sound bearing problem long ago. It turns out that "Mother Nature" has developed a biological system that can not only hear the sound, but can determine the angle from which the sound came.

1. Biological Motivation

There exists a fly, the *Ormia ochracea*, which has ears that are extremely sensitive to the direction of sound and are small enough that they can easily be mimicked within a biomimetic silicon chip.

The genus *Ormia* is a parasitoid and procreates by the female fly laying its larvae on live male crickets [Miles *et al.,* 1995]. Most common hosts are genus *Gryllus or Scapteriscus;* for example in the case of *Ormia ochracea*, it is male field crickets [e.g. *Gryllus firmus*] that are the hosts [Christe, 2003], while with *Ormia depleta*, it is the male mole crickets [e.g. *Scapteriscus borellii*] that are the hosts [Frank *et al.*, 2006]. The larvae then eat the cricket for nourishment in preparation for their metamorphosis [Robert *et al.*, 1994]. However, crickets are

mostly nocturnal and black so the fly cannot rely on its eyesight to find them. Instead it has developed ears that not only hear the male crickets mating call, but also tell the fly the angle the sound came from, so the fly can vector in on the location of the cricket. For ease of understanding the mechanics of the biology, only the species *Ormia ochracea's* ears will be explained, since it will otherwise become too confusing to discuss the minute differences between all the *Ormia* species' ears.

a. Fly's Auditory Mechanics

The fly itself is relatively small, only measuring about a centimeter in length [Christe, 2003]. Because of its small size, the ear structure is not very big either; the ear drums are separated by a mere 500 μm [Christe, 2003]. The ears of the fly are not located on the head as in humans, but instead they are located on the thorax just behind the head [Miles et al., 1995]. Their location along with their small size means that the fly cannot rely on the difference in arrival times and amplitudes of sound at each ear, as most animals do, including humans. Instead the fly developed a unique way of amplifying the arrival time difference and amplitude difference. The fly achieves this difference by mechanically coupling both of its ear drums together via a bridging membrane [Miles et al., 1995].

For those that might enjoy the biological terms and all those scientific names, specific details of the internals of the ear structure can be read about in Robert *et al.* (1994). However, for physics majors, a more basic description of the fly's ears is more appropriate. Looking at the fly's auditory organ, as in Figure 1 below, the ear structure can be broken down into two mechanical bars connected by a hinge membrane [Miles *et al.,* 1995]. Parts 1 and 2 from the picture are the bars, part 3 is the hinge. PTM is prosternal tympanal membrane and for all intents and purposes is the ear drum of the fly and is the mechanism that drives the solid bars via the sound input [Miles *et al.,* 1995].

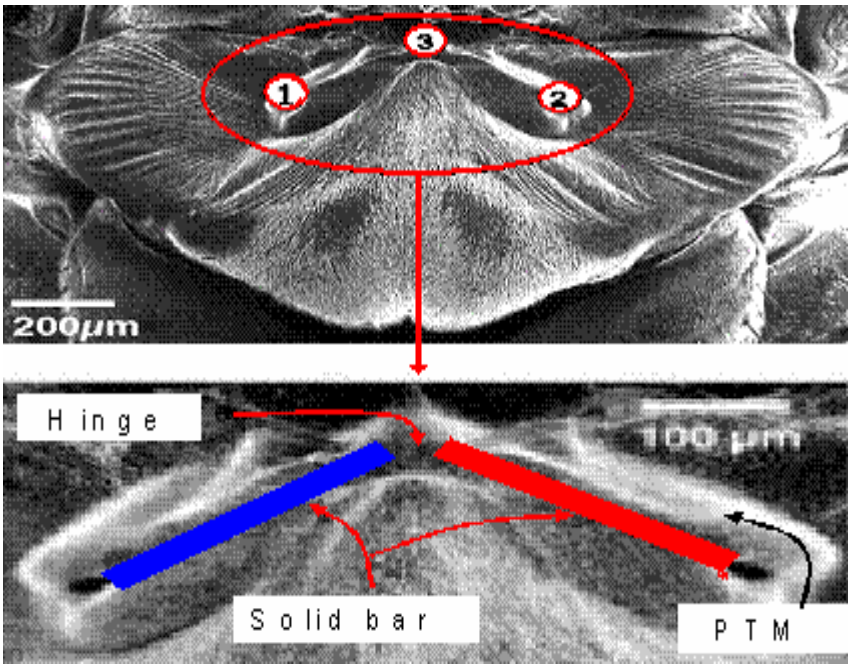

Figure 1. Fly's auditory system and mechanical components (After: Miles *et al.*, 1995).

The key physics behind how the ear structure works so well at determining the angle of incidence is the solid bar and hinge interaction. This interaction can be modeled via a simplified yet accurate mechanical equivalent system.

b. Simplified Mechanical System

A quick glance at this mechanical system makes it seem difficult and overwhelming, but the mechanical system can be simplified into a simple schematic of springs, bars, damping devices, etc. as shown below in Figure 2 [Miles *et al.,* 1995].

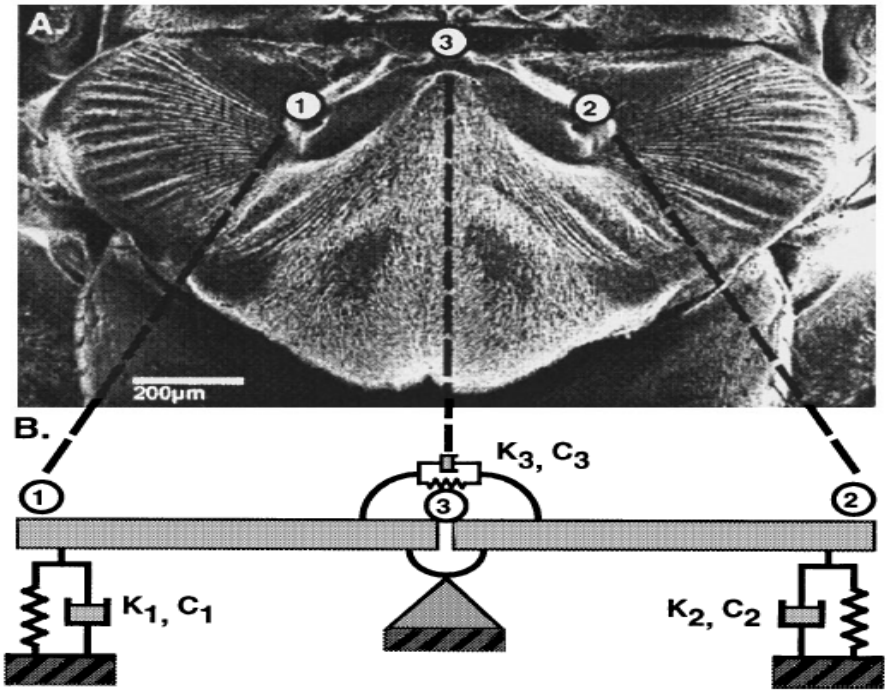

Figure 2. Simplified mechanical equivalent of the fly's ear system (From: Miles *et al.*, 1995).

This is essentially a two degree of freedom spring-mass-damper system with a torsional element. To fully understand the fly's mechanism, a more detailed look into two degree of freedom spring-mass-damper systems is now appropriate.

B. PHYSICS OF WORKING SYSTEM

1. Simple Two Degrees of Freedom Spring-Mass-Damper System

Assume for ease of understanding that the mechanical system of interest is modeled as in Figure 3, a simple two degree of freedom spring-mass-damper system.

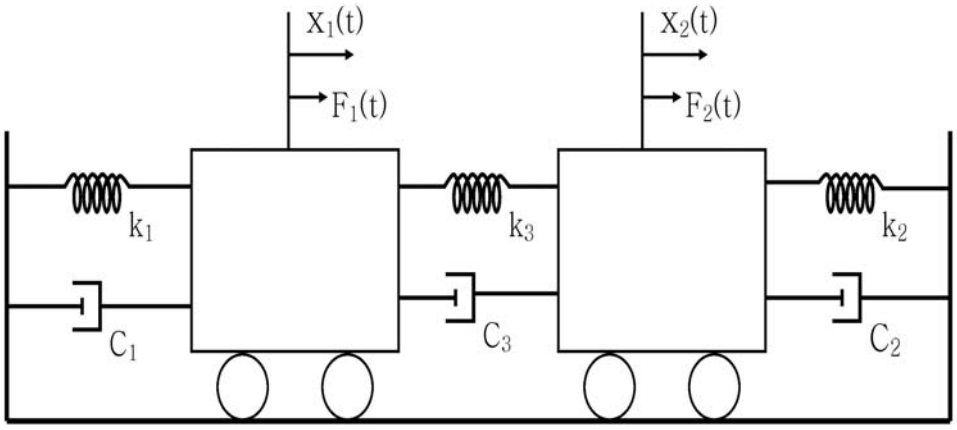

Figure 3. Two degrees of freedom spring-mass-damper system (After: Rao, 2003).

Then the free-body diagrams look like those in Figure 4.

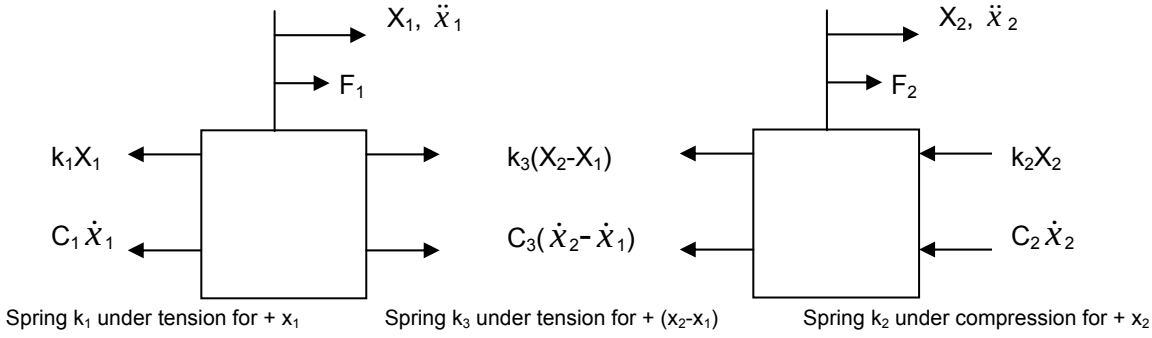

Figure 4. Free-body diagram (After: Rao, 2003).

From these diagrams the equations of motion can be determined applying Newton's second law as discussed by S. Rao [Rao, 2003].

$$m\ddot{\vec{x}} = \vec{F}_{net} \tag{1.1}$$

Think about all the forces on each body in Figure 4 and place them on the right side of the equation. The force due to a spring is opposite in direction and proportional to the displacement; while the damping force is opposite in direction and proportional to the speed. Therefore use the following equations to define the forces.

$$F_{spring} = -kx; \quad F_{damping} = -C\,\dot{x} \tag{1.2}$$

The k is known as the spring constant and the C is known as the damping constant. Thus, the equations of motion for the system in Figure 4 become:

$$m_1\ddot{\vec{x}}_1 = -k_1x_1 - C_1\dot{x}_1 + k_3(x_2 - x_1) + C_3(\dot{x}_2 - \dot{x}_1) + \vec{F}_1 \tag{1.3}$$

$$m_2\ddot{\vec{x}}_2 = -C_3(\dot{x}_2 - \dot{x}_1) - k_3(x_2 - x_1) - k_2x_2 - C_2\dot{x}_2 + \vec{F}_2 \tag{1.4}$$

It is important to note that if the system is moved in the positive X direction then spring k_2 will be under compression and therefore a negative force too. Hence the two damping forces and the two spring forces are negative for equation 1.4, vice the two positive and two negative in equation 1.3, where the springs were both under tension.

Grouping like terms and rearranging, these can be rewritten as [Rao, 2003]:

$$m_1\ddot{x}_1 + (C_1 + C_3)\dot{x}_1 - C_3\dot{x}_2 + (k_1 + k_3)x_1 - k_3x_2 = F_1 \tag{1.5}$$

$$m_2\ddot{x}_2 - C_3\dot{x}_1 + (C_3 + C_2)\dot{x}_2 - k_3x_1 + (k_3 + k_2)x_2 = F_2 \tag{1.6}$$

These are two coupled second order ordinary differential equations and can be expressed in matrix form as [Rao, 2003]:

$$[m]\ddot{\vec{x}}(t) + [C]\dot{\vec{x}}(t) + [k]\vec{x}(t) = \vec{F}(t) \tag{1.7}$$

Where the mass, damping, and spring constant (stiffness) matrices are:

$$[m] = \begin{pmatrix} m_1 & 0 \\ 0 & m_2 \end{pmatrix}; \; [C] = \begin{pmatrix} C_1 + C_3 & -C_3 \\ -C_3 & C_3 + C_2 \end{pmatrix}; \; [k] = \begin{pmatrix} k_1 + k_3 & -k_3 \\ -k_3 & k_3 + k_2 \end{pmatrix}$$

While the displacement and force matrices are:

$$\vec{x}(t)=\begin{pmatrix}x_1(t)\\x_2(t)\end{pmatrix};\quad \vec{F}(t)=\begin{pmatrix}F_1(t)\\F_2(t)\end{pmatrix}$$

The displacements of the two masses are in general expressed as a linear combination of the Eigen modes [Rao, 2003].

The Eigen modes are calculated by solving the differential equation 1.7. To simplify the math and to demonstrate the process, assume there is no damping in equation 1.7. Doing so, equation 1.7 becomes equation 1.8.

$$[m]\ddot{\vec{x}}(t)+[k]\vec{x}(t)=\vec{F}(t) \tag{1.8}$$

Solving the homogenous solution the equation simplifies to equation 1.9.

$$[m]\ddot{\vec{x}}(t)+[k]\vec{x}(t)=0 \tag{1.9}$$

Assuming the solution takes the form of $ae^{i\omega t}$ as is done in Taylor's classical mechanics book, then equation 1.9 becomes equation 1.10 [Taylor, 2005].

$$-\omega^2[m]ae^{i\omega t}=-[k]ae^{i\omega t} \tag{1.10}$$

Cancel like terms from both sides and rearrange to take the form of equation 1.11 [Taylor, 2005].

$$([k]-\omega^2[m])a=0 \tag{1.11}$$

At this point it is apparent that "a" could be zero, but that is a trivial solution. So the next logical solution is that the determinant of $([k]-\omega^2[m])$ must be zero [Taylor, 2005]. The determinant of $([k]-\omega^2[m])$ is $\left(k-m\omega^2\right)\left(k+k_3-m\omega^2\right)$ assuming $k_1=k_2=k$ [Taylor, 2005]. Therefore the first two natural frequencies or Eigen modes are:

$$\begin{aligned}\omega_1&=\sqrt{\frac{k}{m}}\\ \omega_2&=\sqrt{\frac{k+2k_3}{m}}\end{aligned} \tag{1.12}$$

In the following section, the response of the Fly's ears will be analyzed using the above matrix formalism.

2. Fly's Mechanical Model

Just as was done for the simple two degree of freedom example, the first step is to take the mechanical system of the fly in Figure 5 and produce an equivalent free-body diagram. Since the right and left ear structures are the same, $K_1=K_2$ and $C_1=C_2$; it is just easier to call them K_s and C_s (s for structure). In addition k_3 and c_3 where renamed to K_t, C_t due to the coupling membrane (t for tympanal bridge). Notice that the spring K_t expands as and springs K_s get compressed as θ_1 and θ_2 get bigger. This is an important difference from the simple two degree of freedom example in Figure 3.

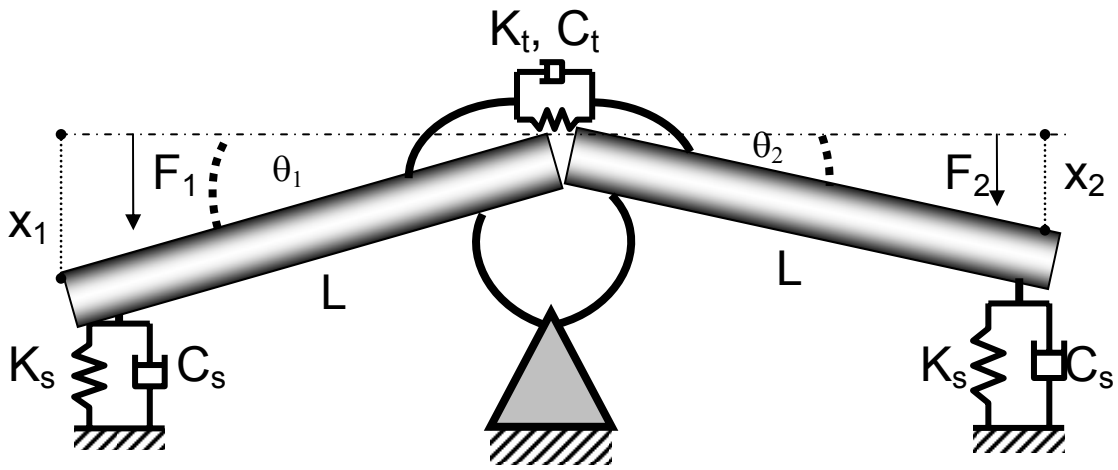

Figure 5. Simplified mechanical equivalent of the fly's hearing System (After: Miles *et al.*, 1995).

The amount of displacement of the fly's ears is very small (nanometer) compared to the length (L) of the bar (millimeter); therefore the small angle approximation applies. That is instead of $X=L*\sin(\theta)$, X can be approximated to be $X = L*\theta$ and the analysis can be done in terms of X vice θ. Keeping the generalized coordinate as X, vice shifting to θ, means that the fly system can be more easily compared to the simple two degrees of freedom example discussed earlier.

Figure 6 is the free-body diagram produced from the mechanical system in Figure 5. Springs K_s where compressed, due to F_1 and F_2, and thus have a restoring force upward. Spring K_t causes a restoring force upward on each bar as well. The damping forces too are upward.

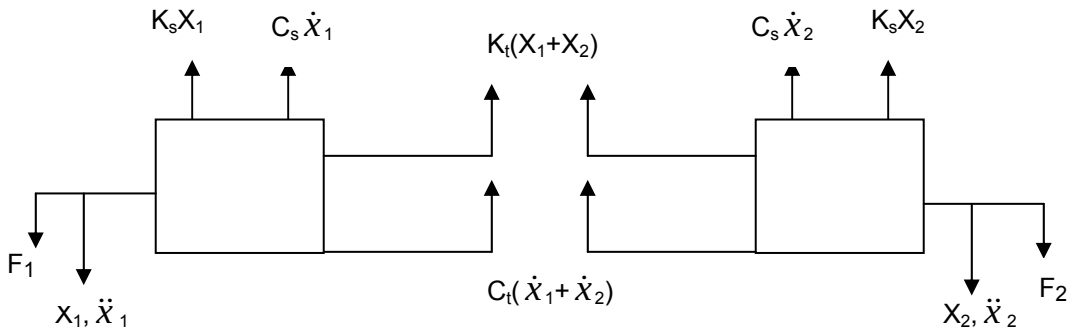

Figure 6. Fly free-body diagram.

The next step is to formulate the equations of motion for the system using Newton's second law again as follows:

$$m_1\ddot{\vec{x}}_1 = -K_s x_1 - C_s\dot{x}_1 - K_t(x_2 + x_1) - C_t(\dot{x}_2 + \dot{x}_1) + \vec{F}_1 \qquad (1.13)$$

$$m_2\ddot{\vec{x}}_2 = -K_s x_2 - C_s\dot{x}_2 - K_t(x_2 + x_1) - C_t(\dot{x}_2 + \dot{x}_1) + \vec{F}_2 \qquad (1.14)$$

Rearranging and grouping like terms as done before in the simple two degree of freedom example, the equations become:

$$m_1\ddot{x}_1 + (C_s + C_t)\dot{x}_1 + C_t\dot{x}_2 + (K_s + K_t)x_1 + K_t x_2 = F_1 \qquad (1.15)$$

$$m_2\ddot{x}_2 + (C_s + C_t)\dot{x}_2 + C_t\dot{x}_1 + (K_s + K_t)x_2 + K_t x_1 = F_2 \qquad (1.16)$$

Since the bars are identical their masses are equal, m_1=m_2, and thus the coupled equations of motion in matrix form becomes equation 1.12 [Miles *et al.,* 1995]. Equation 1.17 is the primary equation for the motion of the fly's ear structure.

$$\begin{bmatrix} m & 0 \\ 0 & m \end{bmatrix}\begin{bmatrix} \ddot{x}_1 \\ \ddot{x}_2 \end{bmatrix} + \begin{bmatrix} C_s + C_t & C_t \\ C_t & C_s + C_t \end{bmatrix}\begin{bmatrix} \dot{x}_1 \\ \dot{x}_2 \end{bmatrix} + \begin{bmatrix} K_s + K_t & K_t \\ K_t & K_s + K_t \end{bmatrix}\begin{bmatrix} x_1 \\ x_2 \end{bmatrix} = \begin{bmatrix} F_1 \\ F_2 \end{bmatrix} \qquad (1.17)$$

The torsional form of this equation is not as straight forward but included here as background for issues relating to inertia to be discussed later. The transformation from equation 1.17 to 1.19 used the following equations:

$$\begin{aligned} X &= L\theta \\ F &= T / L \\ L^2 m &= I \end{aligned} \tag{1.18}$$

By placing the two equations (1.17 and 1.19) close together it is easier to see the translation from mass to inertia and force to torque.

Inertia Damping Stiffness Torque

$$\begin{bmatrix} I & 0 \\ 0 & I \end{bmatrix} \begin{bmatrix} \ddot{\theta}_1 \\ \ddot{\theta}_2 \end{bmatrix} + L^2 \begin{bmatrix} C_s + C_t & C_t \\ C_t & C_s + C_t \end{bmatrix} \begin{bmatrix} \dot{\theta}_1 \\ \dot{\theta}_2 \end{bmatrix} + L^2 \begin{bmatrix} K_s + K_t & K_t \\ K_t & K_s + K_t \end{bmatrix} \begin{bmatrix} \theta_1 \\ \theta_2 \end{bmatrix} = \begin{bmatrix} T_1 \\ T_2 \end{bmatrix} \tag{1.19}$$

3. Eigen Frequency Modes

As was discussed for the simple two degree of freedom system, the fly too has a first and second mode of its natural frequencies. These are called the rocking mode and the bending mode. The rocking mode is called that because the motion of the coupled bar mechanism looks like a seesaw as it rocks back and forth. The bending mode is so called because it looks like a bird bending its wings or flapping its wings for flight. Look at Figure 7 for a visual of the bars at an instance in time for each mode.

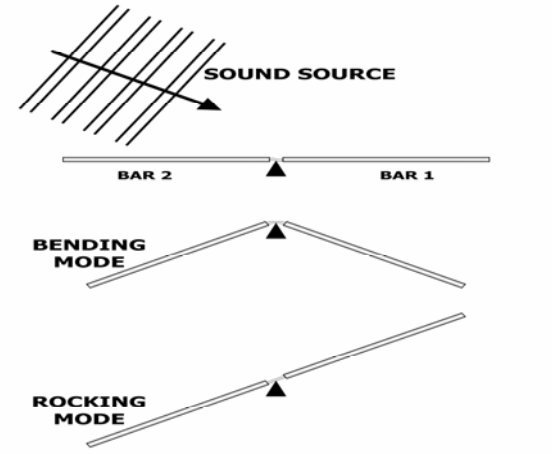

Figure 7. Ear vibration Eigen modes (After: Robert *et al.*, 1996).

a. Rocking Mode and Bending Modes

The Eigen modes of the coupled system can be obtained following the process as described in the two degrees of freedom section but not neglecting damping. The exact solution can be obtained by solving equation 1.17 as described in the Miles *et al* paper. The first two modes are as follows [Miles *et al.,* 1995]:

$$\omega_{Rocking} = \sqrt{\frac{K_s}{M}} \tag{1.20}$$

$$\omega_{Bending} = \sqrt{\frac{K_s + 2K_t}{M}} \tag{1.21}$$

The rocking motion depends only on the two springs at the edges in Figure 5, while the bending motion involves springs at the edges as well as at the center.

4. Displacement due to Sound

Which mode is activated during oscillations of the structure is purely dependent on the initial conditions. For example, if the sound is incident from directly above the structure where the angle of incidence is zero, only the

bending mode can be actuated. However, the most probable situation is that initial conditions are such that linear combinations of the two modes occur simultaneously.

If the sound is incident from the left at an angle as shown in Figure 7, the left ear structure is undergoing a linear combination of the rocking and bending modes. The displacements due to these two modes add together to create a large amplitude on the left side. While for the right ear structure, the rocking mode pushes the right bar up and the bending mode moves it down. These two subtract from each other creating small amplitude on the right ear. The net result is a difference in amplitudes depending on the angle of incidence of the sound.

Expressing this in equation form the linear combination becomes equations 1.22 and 1.23 for the left (x_1) and right (x_2) respectively [Miles *et al.,* 1995]. The subscript b is for bending mode, r is for rocking mode, and ω is the excitation frequency.

The amplitudes of the displacement for each mode are expressed in equations 1.24 and 1.25 [Miles *et al.,* 1995]; m and s are the mass and area of the ear structure, τ is the time delay between the sound force on the left and right bar, and finally P is the amplitude of sound pressure which hardly varies across the fly's ear. The specific derivation was given by Miles *et al, 1995.* Modifying their equations the phase constants for rocking and bending modes can be expressed in terms of a damping coefficient γ.

$$x_1(t) = A_b \sin(\omega t + \phi_b) + A_r \cos(\omega t + \phi_r) \quad (1.22)$$

$$x_2(t) = A_b \sin(\omega t + \phi_b) - A_r \cos(\omega t + \phi_r) \quad (1.23)$$

$$A_r = \frac{Ps}{m}\left(\frac{\sin(\omega\tau/2)}{\sqrt{\left(\omega_r^2 - \omega^2\right)^2 + \left(\gamma_r \omega\right)^2}}\right) \quad (1.24)$$

$$A_b = \frac{Ps}{m}\left(\frac{\cos(\omega\tau/2)}{\sqrt{\left(\omega_b^2-\omega^2\right)^2+\left(\gamma_b\omega\right)^2}}\right) \quad (1.25)$$

$$(\phi_r) = arc\tan\left(\frac{\gamma_r\omega}{\left(\omega_r^2-\omega^2\right)}\right) \quad (1.26)$$

$$(\phi_b) = arc\tan\left(\frac{\gamma_b\omega}{\left(\omega_b^2-\omega^2\right)}\right) \quad (1.27)$$

Typical values of the parameters for this mechanical model of the fly come from the Miles et al., 1995, paper. Using these values, the amplitudes of oscillation for the right and left ears based on equations 1.21 and 1.22 were calculated using MATLAB. Figure 8 shows amplitudes and phases of the left and right ears as a function of sound frequency. In this analysis sound is assumed to be incident at 45 degrees with a pressure of one Pascal.

For example, a 5 kHz sound wave, which arrives at both ears with the same magnitude, is detected with approximately a 10 dB magnitude difference by the fly's ears [Karunasiri *et al.,* 2005].

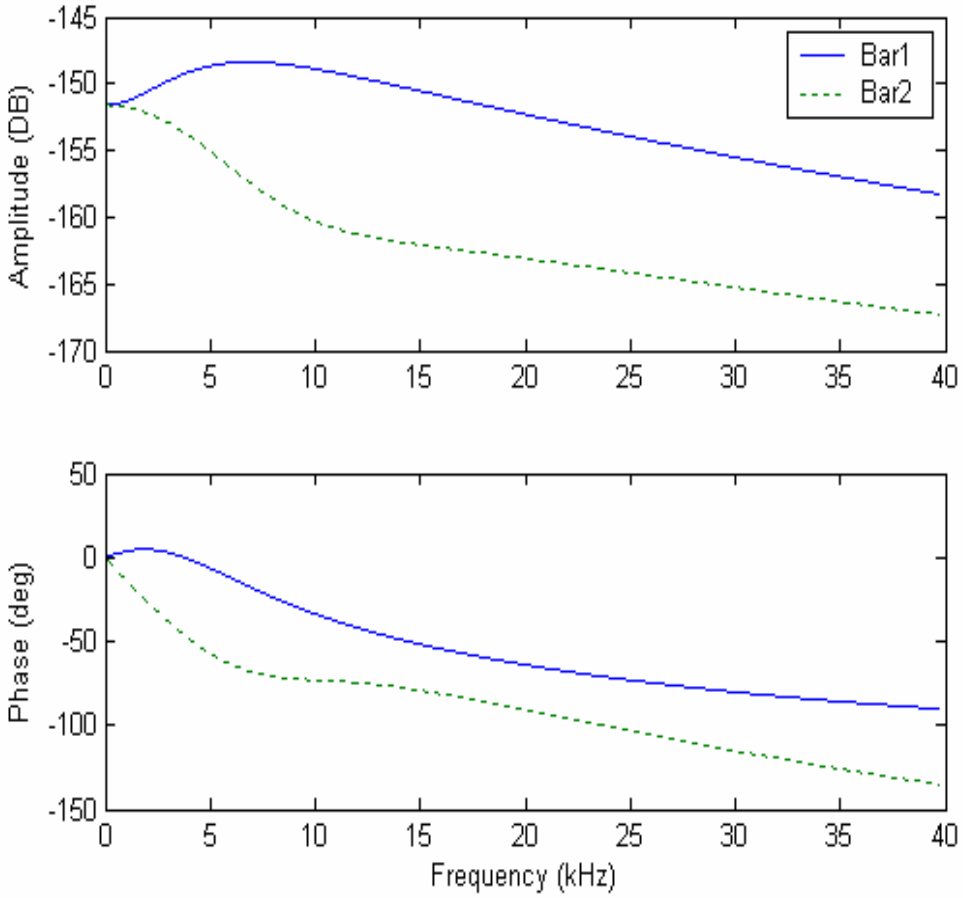

Figure 8. Frequency response of the ears based on the model (From: Karunasiri *et al.,* 2005).

Figure 9 shows the time dependence of oscillations with relatively large amplitude difference created when the incident sound comes from a 45 degree angle. The phase shift is clearly visible from the two traces in Figure 9.

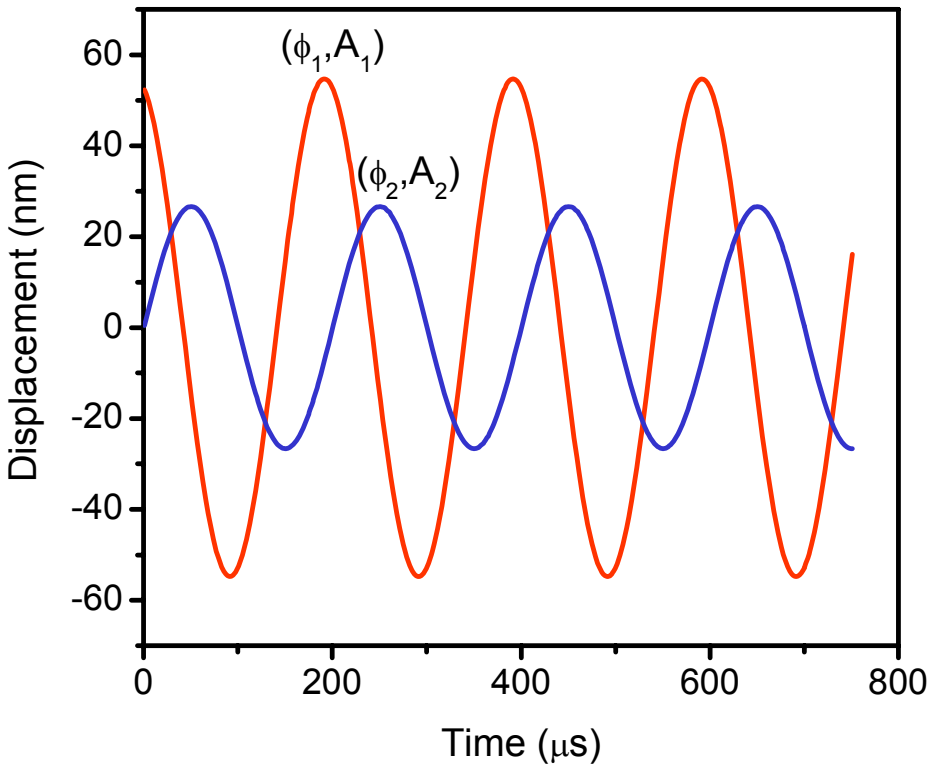

Figure 9. Transient response based on the model for 45 degree inclined 5kHz sound wave (After: Karunasiri *et al.,* 2005).

Analytical expressions of the two amplitudes oscillation in Figure 9 can be obtained using the two Eigen modes. The displacements of the two sides can be written as:

$$x_1(t) = A_1 \sin(\omega t + \phi_1) \tag{1.28}$$

$$x_2(t) = A_2 \sin(\omega t + \phi_2) \tag{1.29}$$

where A_1 and A_2 are the amplitudes of the left and right ears and ϕ_1 and ϕ_2 are the corresponding phases. Using equations 1.22 to 1.29, it can be shown that the two amplitudes and phase difference are given by:

$$A_1^2 = A_b^2 + A_r^2 + 2A_bA_r\sin\left(\phi_b - \phi_r\right) \quad (1.30)$$

$$A_2^2 = A_b^2 + A_r^2 - 2A_bA_r\sin\left(\phi_b - \phi_r\right) \quad (1.31)$$

$$\cos\left(\phi_2 - \phi_1\right) = \frac{A_b^2 - A_r^2}{A_1A_2} \quad (1.32)$$

It can be easily seen that the amplitude ratio and phase difference are independent of the incident sound pressure.

5. Determination of the Direction of Sound

It has been shown that the fly's mechanical system responds with a difference in amplitude for the side that the sound is incident from, it is also important to discuss that there is an amplification in the sensed time difference of arrival of the sound waves too.

a. Sensed Time Difference

If the fly did not amplify this signal, the time arrival difference would only be approximately 2.5 micro seconds [Karunasiri *et al.,* 2005]. This is too small for the fly to notice an appreciable difference. However, according to Figure 9, there is a large phase difference between the left and right ears. This phase difference corresponds to a sense time difference of about 50 microseconds [Karunasiri *et al.,* 2005]. That corresponds to an amplification of 20 times. Figure 10 shows the amplification of the sensed time difference for different frequencies.

What is most noticeable is the linear region from -40 to +40 degrees for 5 kHz tonal. It is no coincidence that biology has evolved the parasitic fly's ears to the tonal frequency for the cricket host. The fly shows excellent directionality for this region of incident angles and can thus vector in easily on its prey.

So if the frequency of the incoming signal is known, and the time difference is sensed, then it is possible to derive the angle of incident sound using equation 1.33, with relative ease.

$$(t_2 - t_1) = \frac{1}{\omega}\cos^{-1}\left[\frac{A_i^2 - A_r^2}{A_1 A_2}\right] \tag{1.33}$$

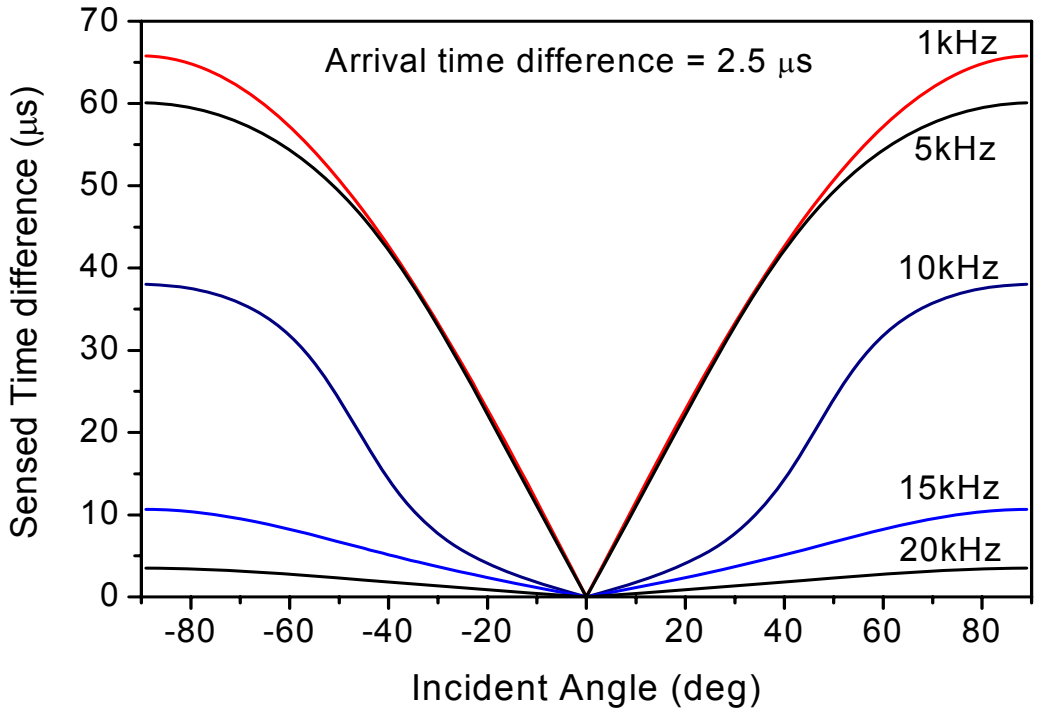

Figure 10. Sensed time difference for different frequencies and angles.

C. MATLAB PROGRAM TO VISUALIZE SYSTEM WORKING

In order to visualize the fly's bars in action, a MATLAB simulation program was created using the equations from the Miles *et al.*, 1995, paper and the parameter values from the Roberts *et al.*, 1994, paper. Code for the MATLAB program is contained in Appendix A, so that the program can be run and seen working with the ear bars actually moving, if so desired.

1. Sound from Zero Degrees

Figures 10, 11, and 12 show the bars at chronological instances in time for sound incident from zero degrees. They are actual screen shots while the program was running in a PowerPoint presentation. Notice that there is no amplitude difference between the left (blue) and right bars (red).

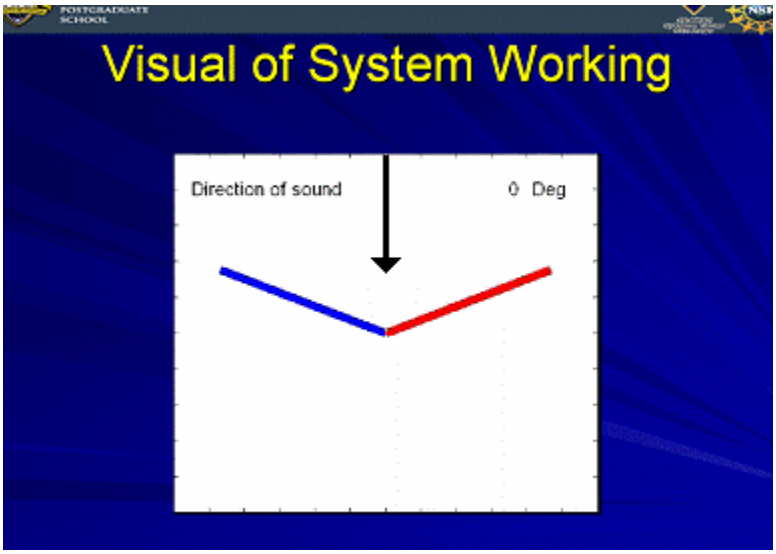

Figure 11. Zero degrees incidence with bars up.

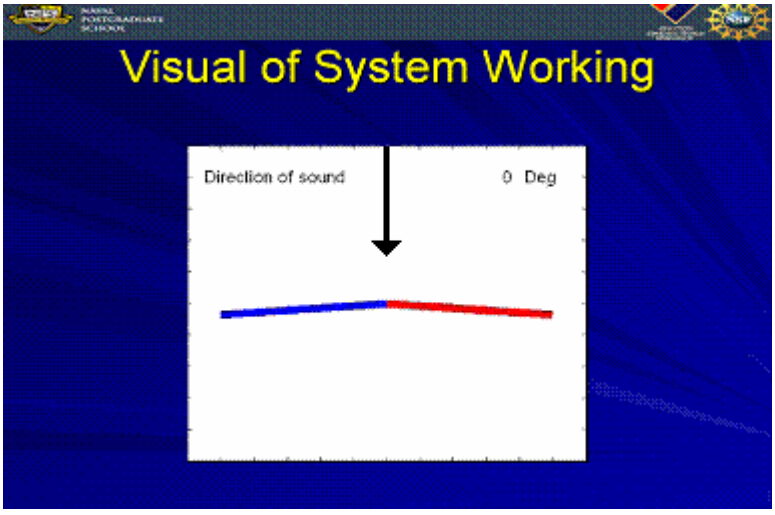

Figure 12. Still zero degrees and the bars moved down.

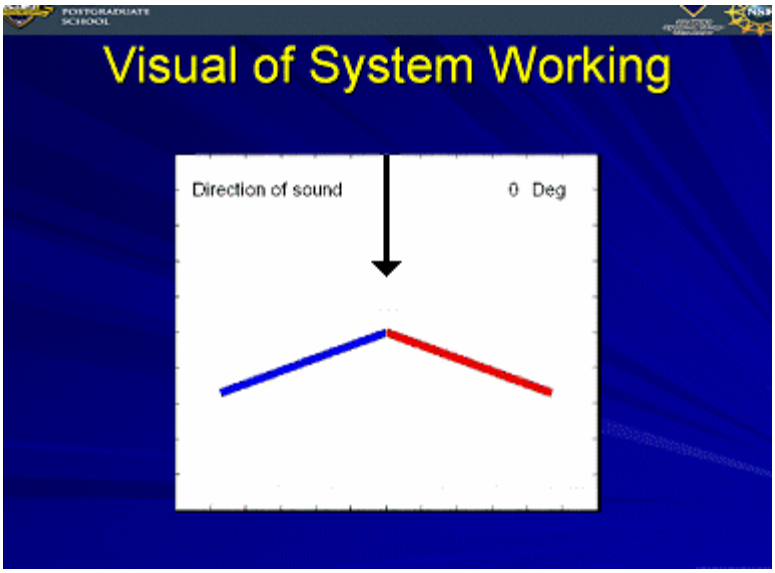

Figure 13. Zero degrees and bars moved completely down.

The motion depicted in the transition from Figure 11 to Figure 13 is the bending mode and the animation looks like a bird flapping its wings. Again notice that as the wings flapped, the amplitude on each side was the same.

2. Sound from 30 Degrees

Figures 14, 15, and 16 show the same chronological transition in time but for sound incident from 30 degrees. Here the motion will not be pure bending mode, but a linear combination of the rocking mode and the bending mode. It looks like the wings are flapping, but the right wing flaps with a higher amplitude and phase.

Note that in this MATLAB program the sound is coming from the right, unlike diagram in Figure 7. Because of this, the right or red bar will have the higher amplitude and phase.

The screen shot, Figure 14, was taken as close in time as possible to the two bars at the horizontal position. Screen shots are taken while the program is running and the bars are in motion.

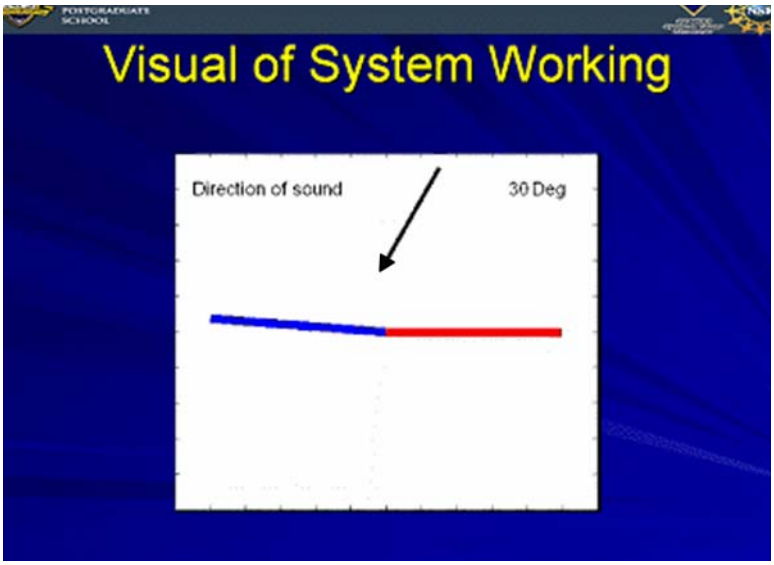

Figure 14. 30 degree incident sound with bars horizontal.

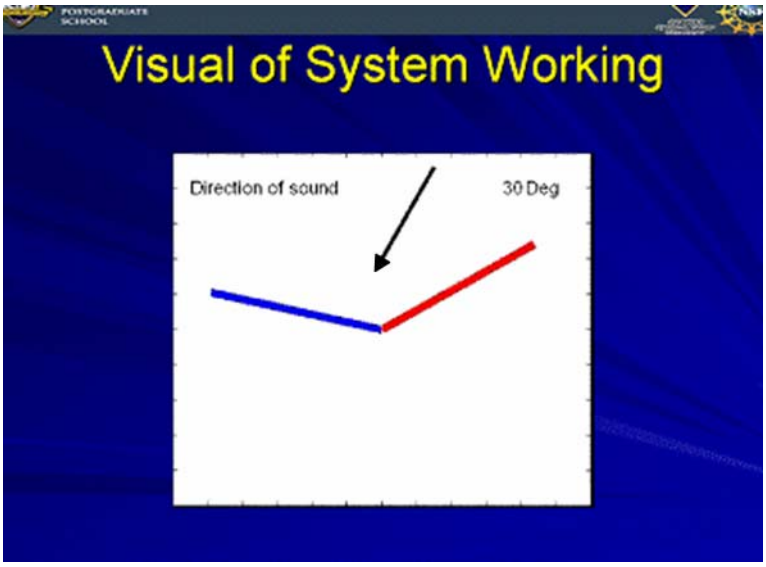

Figure 15. 30 degree incident sound with bars up – red bar higher amplitude.

It is difficult to see in these transition slides, but the red bar also has phase difference which translates to a slight speed difference in the oscillations.

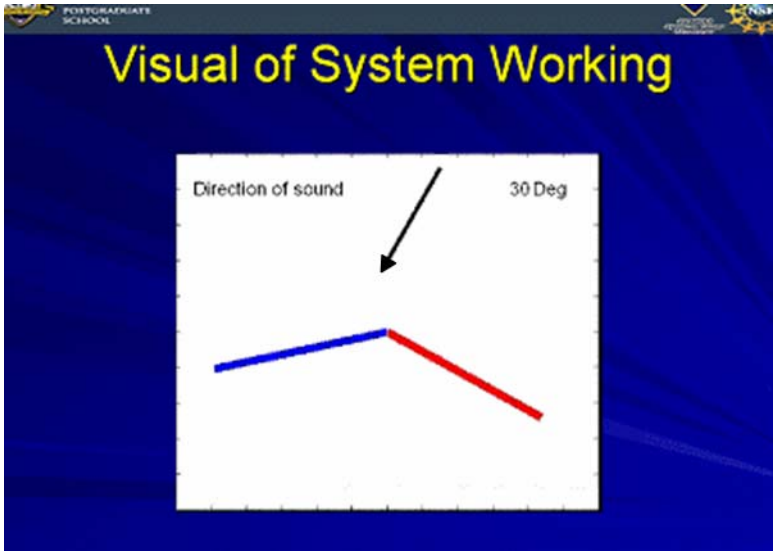

Figure 16. 30 degree incident sound with bars down– red bar higher amplitude.

3. Sound from 60 Degrees

This amplitude and phase difference is even more noticeable at 60 degrees incident angle.

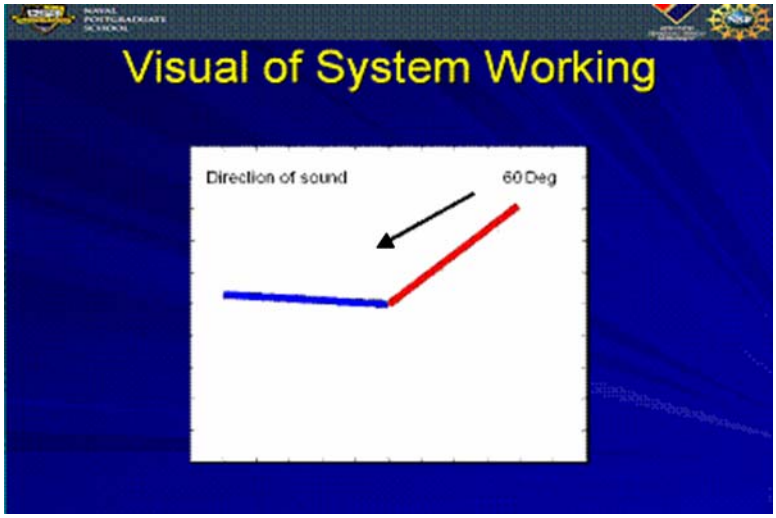

Figure 17. 60 degree incident sound with bars down–red bar highest amplitude.

II. BIOMIMETIC MEMS DESIGN

Biomimetics is the study of nature and the attempt to mimic that nature in man made devices. After all, no matter what religion or belief system one might hold, nature has at least a few thousand year head start on the production of complicated organisms than man does. This time advantage has most often lead to incredibly efficient devices worth mimicry. In the previous chapter it was shown that biology has developed a sound sensing organ capable of determining the bearing that the sound came from.

MEMS stands for Micro-Electro-Mechanical System and "… is the integration of mechanical elements, sensors, actuators, and electronics on a common silicon substrate …" [MEMSNET, 2007]. Not only are there moving parts at the micro scale, but there exists the ability to electrically connect to those parts so that a sensor can be built and readout achieved. Given the micrometer size of the fly's ear structure, MEMS is the perfect medium with which to create the biomimetic sound sensor.

A. MERITS OF THE POLYMUMPS PROCESS

Previous investigators have attempted to mimic this fly's hearing organ in silicon devices before; for examples see the Yoo *et al.* (2002), and Cui (2004), papers. However, many of the silicon-device building processes were custom processes and therefore costs reflected those specialized processes.

MUMPs® stands for Multi-User MEMS Processes. The key to lowering the cost of devices is to try to use one of the existing standard processes. PolyMUMPs is one of those existing processes. It stands for Polysilicon Multi-User MEMS Processes. According to MEMSCAP, the owners of the process, PolyMUMPs is a "… three-layer polysilicon surface and bulk micromachining process, with two sacrificial layers and one metal layer…" [MEMSCAP, 2003].

The PolyMUMPs process helps to lower the cost because hundreds of different chips can be integrated in the same batch process. In addition, the layers of metals and silicon within the existing process definition allow for easy electrical access to the moving mechanical parts to achieve the readout necessary for the sensor to work.

1. PolyMUMPs Process Definition

In order to fully understand the MEMS device design, first a discussion about each of the different layers of the PolyMUMPs process is required.

Each chip starts with a silicon substrate. The substrate acts as the foundation on which the structure is built. It is approximately 400 micrometers in depth.

On this foundation a 0.6 micrometer of nitride is grown. The purpose of the nitride is to electrically isolate the substrate from the structure above.

Next a layer of 0.5 micrometer polysilicon is grown, called Poly Zero. Polysilicon is silicon in which there is no preferred orientation in which the crystals are grown. This means that it has slightly different chemical characteristics from the silicon used in the substrate which is single orientation crystalline silicon. Poly Zero layer is typically used for electrical contacts, but can be designed to be used for any other purpose. In the case of the sound sensor built, this layer was used for electrical contacts

After the Poly Zero, a layer of photo resist is laid down. Photo resist is a chemical that when exposed to ultraviolet light will change its chemical characteristics. This change in chemical characteristics allows the use of a pattern mask so that designs can be placed onto the photo resist. Then the system is dipped in a chemical bath or reactive ion field that removes the photo resist and Poly Zero in the areas not exposed to light. All that is left then is the patterned Poly Zero and the exposed photo resist. A bath in a different solution removes the photo resist.

Then a layer of Oxide (SiO_2) is laid down. This oxide layer is two micrometers thick. The oxide is patterned using photo resist and a mask following the same basic process as before. The purpose of the oxide layer is usually to provide a temporary space and later will be chemically removed to allow for structure to be free released and able to move.

The next step is another layer of poly silicon. This layer is called Poly One and is also two micrometers thick. Again a process of photo resist, masking, and chemical etching a design takes place. In the built sound sensor the Poly One layer was the bottom layer of the bar-hinge-bar system mimicking the fly.

On top of the Poly One layer a second oxide layer is placed. Only this oxide layer is only 0.75 micrometers thick. It follows the same processes as the first oxide layer and is typically used for the same purposes.

Following patterning of oxide two, a third layer of polysilicon, called Poly Two is laid. At 1.5 micrometers thick it too is patterned and etched following the same processes described before. In the sound sensor this layer served as the top layer of the bar-hinge-bar structure.

The final layer is 0.5 micrometers of gold placed on top of the Poly Two layer and then patterned and etched in similar style as before. The gold layer is most often used for electrical contacts.

Figure 18 shows the layers in their order and shows thicknesses as well. The substrate and nitride are not shown, as they are only the foundation.

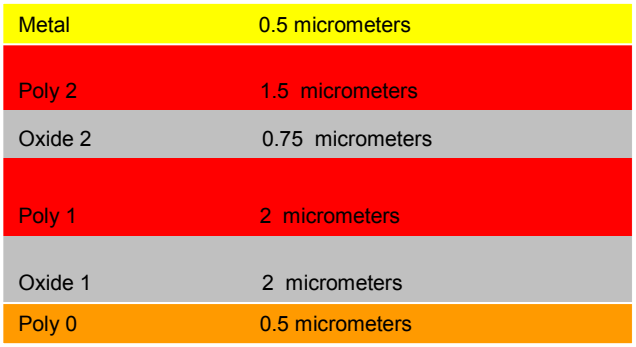

Figure 18. PolyMUMPs layering and thicknesses (After: Koester *et al.*, 2003).

A more detailed description of how the layers in the PolyMUMPs process are created can be found in the PolyMUMPs Design Handbook [Koester *et al.*, 2003]. However, enough of the basics were described here so that the MEMS biomimetic bar-hinge-bar sound sensing device can be discussed in detail next.

B. BIOMIMETIC MEMS DESIGN

In the fly, the tympanal membrane or ear drum, translated the sound pressures into displacement of the bars. So the silicon device too needed to translate from sound pressure to a displacement. The schematic of the MEMS structure mimicking the fly's ears is shown in Figure 19.

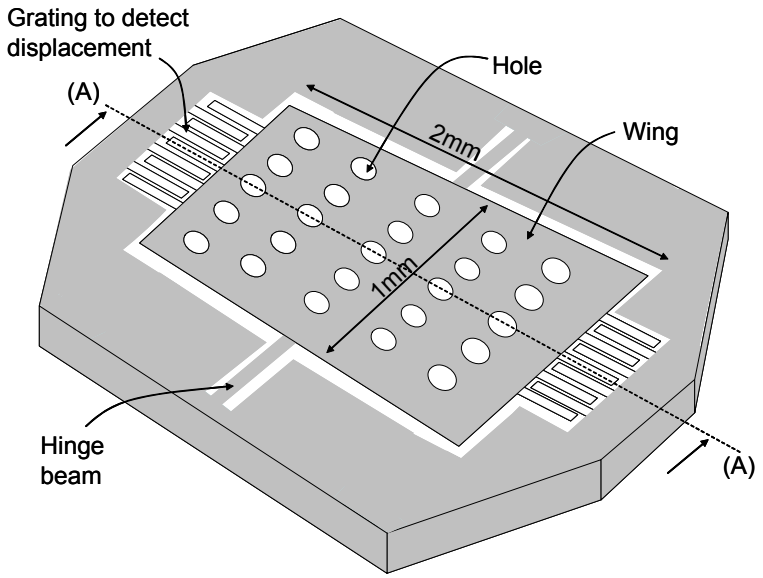

Figure 19. Schematic diagram of fly ear using MEMS (After: Karunasiri *et al.*, 2005).

The basic design of the structure using PolyMUMPs is depicted in Figure 20. There are membranes that act like the bars and the tympanal membranes in the fly's ears. The membranes, which are often referred to as "wings" since they resemble bird wings flapping during the bending mode, are attached to the substrate via a support block. The membranes have holes in them attempting to control the damping of the system as the wings move (C_s). The cantilever beams connecting the support block and the wings act as the springs K_s. Again K_t and C_t

are from the material properties of the polysilicon and are adjusted by the amount of silicon placed in the center of the structure. Initial research, by Dr. Kim, proved that a design of 1000 μm by 2000 μm size plate was the best for proper operation.

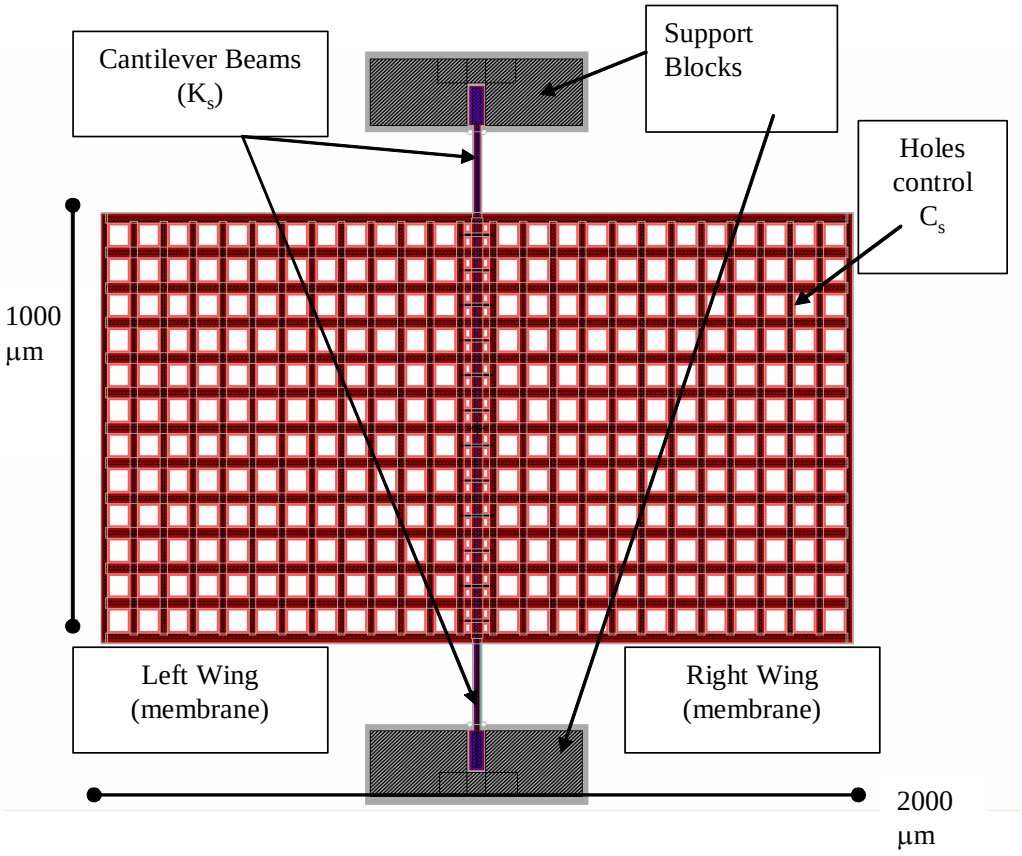

Figure 20. PolyMUMPs design of directional sensor.

What is difficult to see in Figure 20 is the small air gap underneath the device. In addition, it is hard to see what material each part is made from. Figure 21 shows a side view of a typical device showing relative depth.

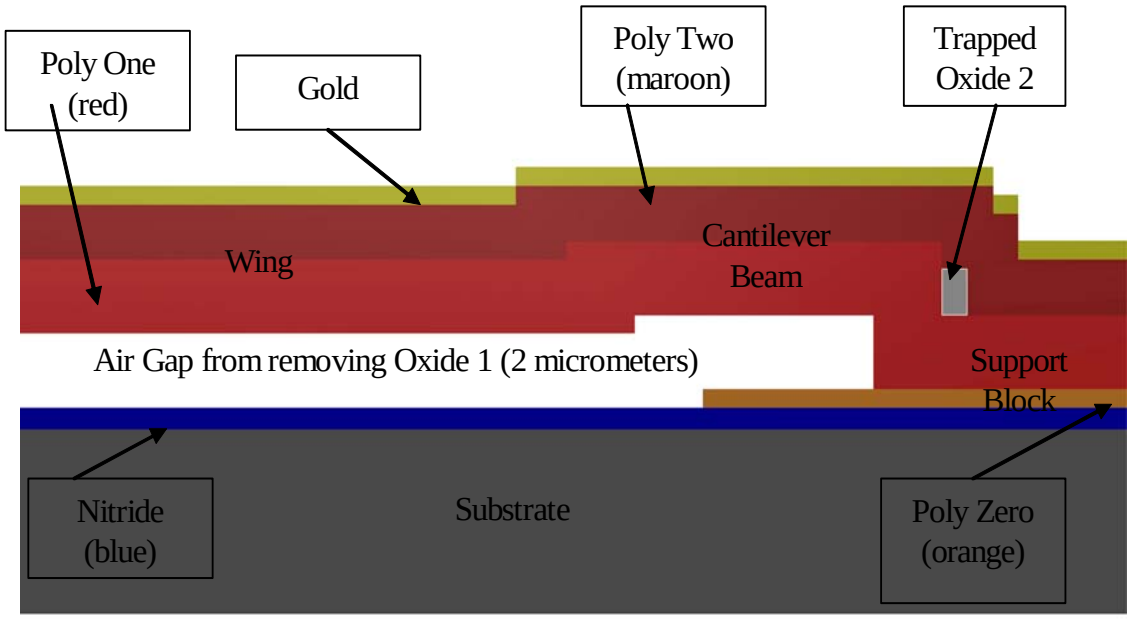

Figure 21. Depth view of a typical PolyMUMPs design.

When the wing structure moves, the small air gap causes a phenomenon, called squeeze film damping. Squeeze film damping is basically a damping force that is felt on the wing structure due to the air trying to escape from underneath the wing as it moves down. If no holes are placed in the plate, then this damping force can be very strong and rendering the plate immovable, in other words, the plate does not react to sound. If there are too large of holes, or too many holes, then this lack of damping force can cause the structure to oscillate too much. Early on into the research, it became apparent that controlling the damping would be important to causing the two modes of operation, rocking and bending, to be as far apart and distinct as possible. Thus multiple device designs, each with different hole sizes and number of holes were created. Each of these different designs was based on a primary design with slight modifications in an attempt to find the optimum configuration.

1. The Primary Design

Figure 22 shows the primary design. The device is smaller than the device in Figure 20, because additional simulation proved that for a 3.5 micrometer thick wing structure, a device approximately 1080 by 1080 micrometers would work better; achieving a rocking and bending frequencies that were farther apart, with higher amplitudes. The 3.5 micrometers comes from two micrometers of Poly One plus 1.5 micrometers of Poly Two. The cantilever beams were simulated for a length of 75 micrometers and a width of 14 micrometers. This proved to be a good size to get a rocking mode of approximately 3 kHz and a bending mode of approximately 6.8 kHz. The holes are 86 micrometers square and there are four rows of nine per wing structure. The small holes in the center are to aid in Oxide layer release.

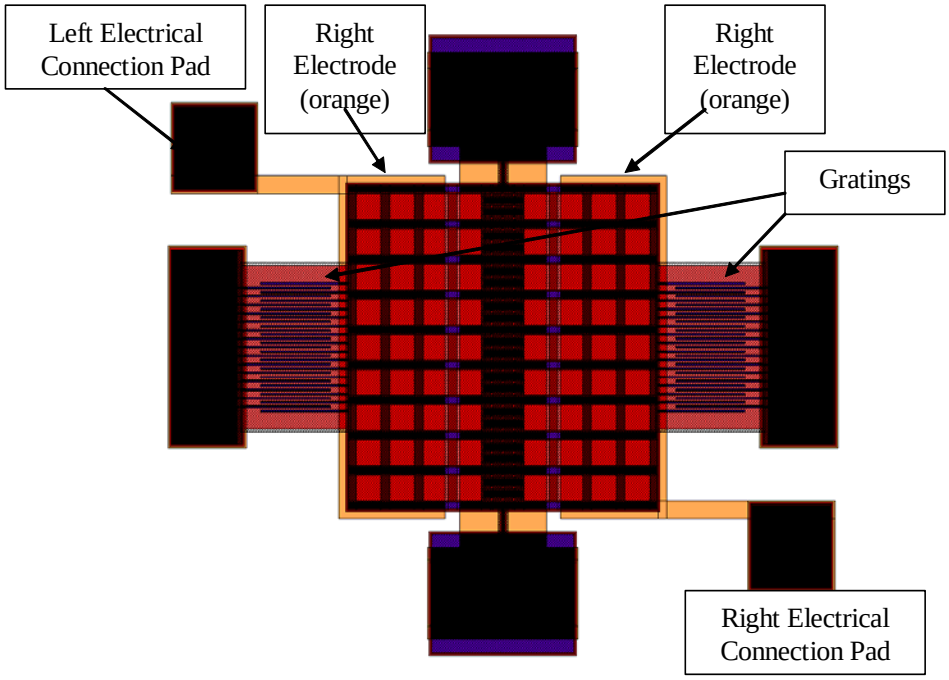

Figure 22. Primary PolyMUMPs design.

If a comparison of Figure 20 and Figure 22 is made, it is quite obvious that a few additional components were added to the initial design.

a. Reasons for Additional Components

Figure 23 shows the electrodes that were added to the structure. They are made out of the Poly Zero layer. The purpose of the electrodes was two fold: First, they were added to be able to electrostatically actuate the device for proof of the rocking mode and bending mode operation of the device. This was achieved by applying an electrical signal to either the left or right electrode, and ground to the center electrode which is connected to the wings via Poly One and Poly Two. Results of this testing will be discussed in more detail in Chapter IV. Second, although not originally planned for, they were utilized in order to retrieve the displacement of the device by measuring the capacitance of the wing-air-electrode (plate-dielectric-plate) of the right or left side. The displacement is proportional to the capacitance. A more detailed discussion of this capacitance measurement system will be discussed in Chapter IV.

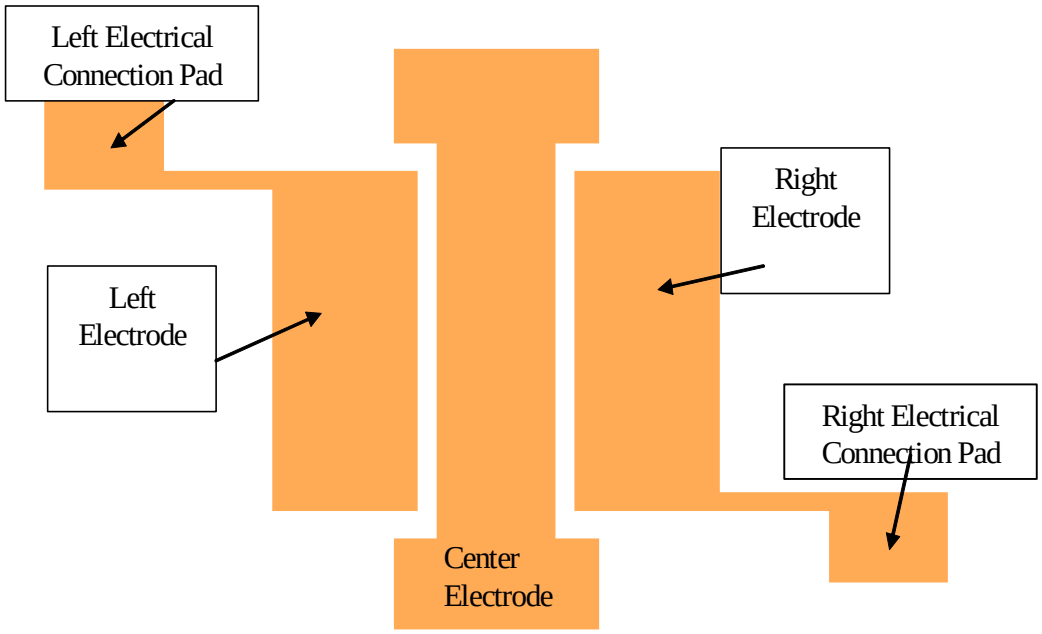

Figure 23. View of primary device electrodes.

Additionally, there were diffraction grating "fingers" added to the device; a set of moveable grating fingers and a set of stationary fingers. Figure 24 shows the gratings up close. The moveable fingers are attached to the left and right wings and will move with the wings as they rock and bend. The stationary fingers are attached to their own support structure and do not move.

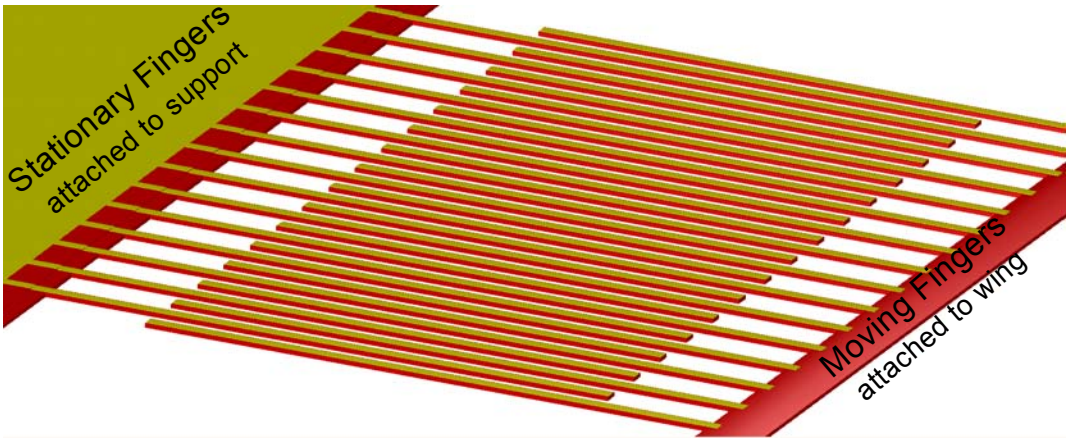

Figure 24. View of grating structure attached to a wing.

The purpose of the diffraction grating is to measure accurately the displacement of the wings. A near infrared laser is shined on the fingers and reflected by the gold on top of the grating fingers. The diffraction pattern is measured by a detector as shown in Figure 25. The displacement can be measured down to less than a nanometer using this method.

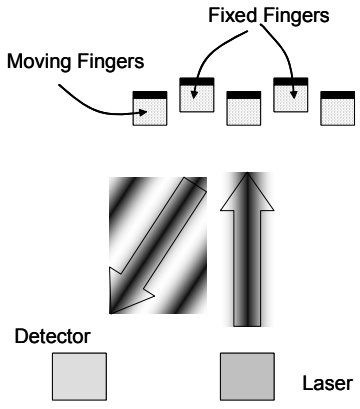

Figure 25. Workings of diffraction grating (From: Kim *et al.*, 2005).

b. 3D View of Primary Device (without Electrodes)

Figure 26 shows the primary device in three dimensions. This view makes it easier to see the device. The electrodes, which are normally underneath the wings and underneath the center, were removed to make it easier to see the damping holes. The red is the polysilicon layers and the yellow is the gold layer.

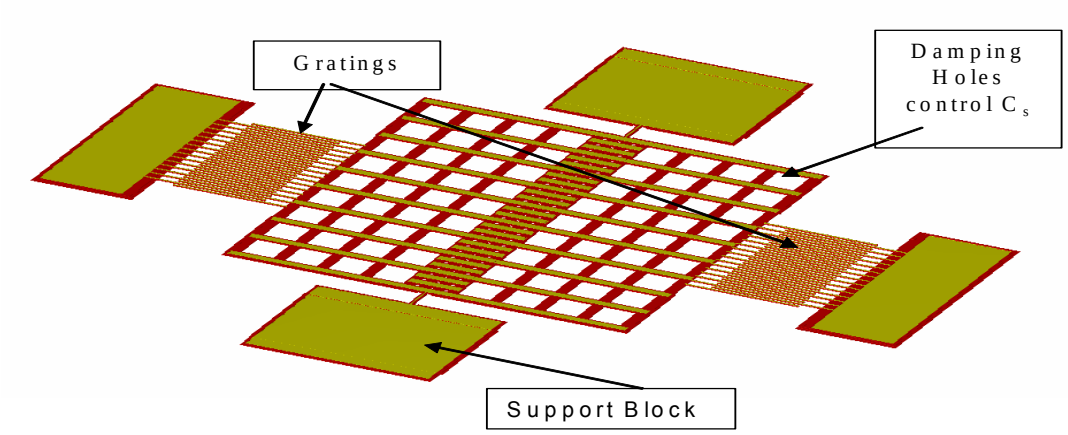

Figure 26. 3D View of primary device without electrodes.

C. CHIP LAYOUT

Proper damping in this device is very crucial to the success of accurately determining the bearing of the sound source. Because of this, it was necessary to try multiple designs to physically see which combination of hole size, number of holes, length of cantilever beam, etc. provided the best performance.

Therefore, 21 different designs were placed on a single chip. Figure 27 shows the layout of all of the devices.

Device number one is the primary design discussed earlier. Deviating from this design, device two has larger holes. Device number three has smaller holes. Testing the effect of beam length on the device, device number four has a smaller cantilever beam. Device number five has a longer cantilever beam.

Combinations of changes occurred too, for example, device number six has larger holes and a shorter beam. These changes are summed up in Table 1.

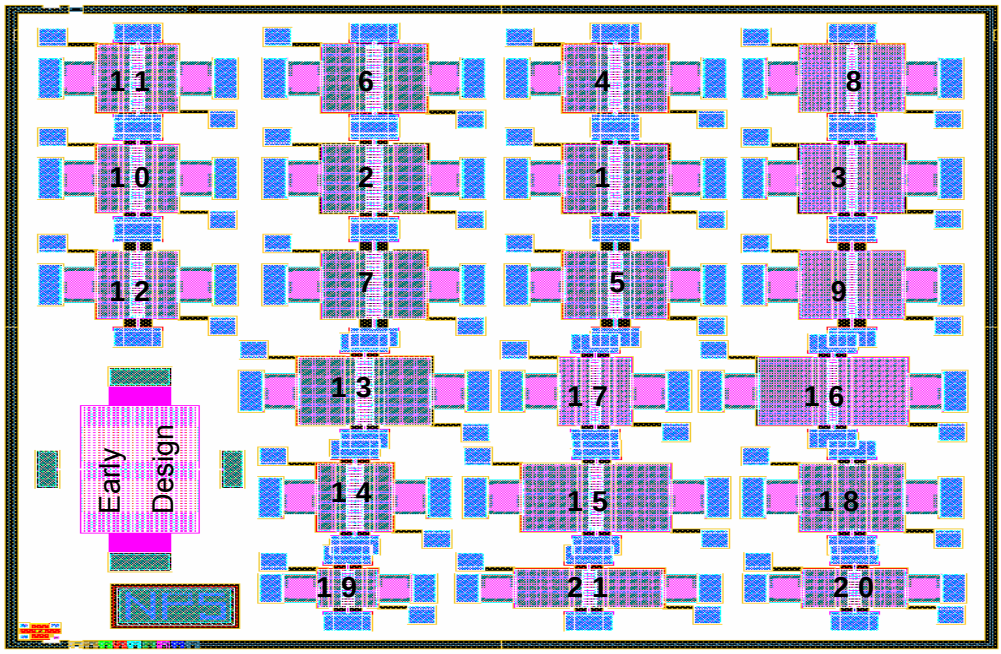

Figure 27. Chip layout.

DEVICE			CANTILEVER BEAM		HOLES	
Number	Length (µm)	Width (µm)	Length (µm)	Width (µm)	Number per wing (across x down)	Square hole Length (µm)
1	1080	1080	75	14	4 x 9	86
2	1080	1080	75	14	3 x 7	120
3	1080	1080	75	14	6 x 13	50
4	1080	1080	37.5	14	4 x 9	86
5	1080	1080	150	14	4 x 9	86
6	1080	1080	37.5	14	3 x 7	120
7	1080	1080	150	14	3 x 7	120
8	1080	1080	37.5	14	6 x 13	50
9	1080	1080	150	14	6 x 13	50
10	850	1080	75	14	3 x 9	86
11	850	1080	37.5	14	3 x 9	86
12	850	1080	150	14	3 x 9	86
13	1380	1080	75	14	4 x 7	120
14	780	1080	75	14	2 x 7	120
15	1540	1080	75	14	6 x 9	86
16	1550	1070	75	14	9 x 13	50
17	750	1070	75	14	4 x 13	50
18	1080	1080	75	14	4.5 x 9 (holes in center column too)	86
19	610	610	75	14	2 x 5	86
20	1080	610	75	14	4 x 5	86
21	1540	610	75	14	6 x 5	86

Table 1. Design parameters used for the chip in Figure 27.

In the next chapter, the simulation of the devices will be discussed using the previous table of design parameters.

III. *COMSOL* MODE SIMULATION

Simulations of the sensors designed in Chapter II were conducted both in *ANSYS* and *COMSOL Multiphysics* finite element modeling (FEM) programs. *ANSYS* simulations were conducted prior to the manufacturing of the devices mostly because it was the FEM program used by the MEMS department at Naval Postgraduate School at that time. However, during the project, the FEM program *COMSOL Multiphysics* was introduced to the project team. *COMSOL* is much easier to use than *ANSYS* and provides similar results. Therefore all simulations after that point were done in the *COMSOL Multiphysics* program.

The *ANSYS* simulations were completed using a code written by Dr. Byungki Kim. A sample of this code is contained in the Appendix B for reference.

Given the comparable results between the two FEM programs, and *COMSOL*'s ability to allow the user to easily add squeeze film damping and sound actuation to this truly multi-physics problem, made *COMSOL* the clear choice for all simulations.

A. *COMSOL* MODE SIMULATION PROCESS

All the *COMSOL Multiphysics* simulations follow the same basic processes. The process is as follows: draw an object, assign some relevant physics equations, designate the materials it is made of, establish boundary conditions, mesh the object, set the solver parameters, and then finally solve the simulation. In many cases the order in which these steps are conducted is not important, but it makes it easier not to skip a step if the same routine is followed every time. The only step for which order matters is the solve step, it must be last.

First, either a 2D image was drawn manually or imported from a Computer Aided Drafting (CAD) program. Then the 2D image was extruded to a 3D image with the proper depth, 3.5 micrometers in this case. 3.5 micrometers was the

sum thickness of the Poly One and Poly Two layers, which comprised the wing structure. Sometimes drawing in 2D and then extruding to 3D is much easier than attempting to draw the device in 3D from the start.

After extrusion, the relevant physics were chosen. In this case since the project team is attempting to determine the Eigen frequencies of the structure, structural mechanics was chosen; specifically the MEMS solid, stress-strain option.

After selecting the physics, the construction material types were chosen. For this simulation the entire structure was Polysilicon.

Boundary conditions for these simulations were straightforward. All portions of the device except the ends of the cantilever beams were free to move. The ends of the cantilever beams were fixed, illustrated in Figure 28.

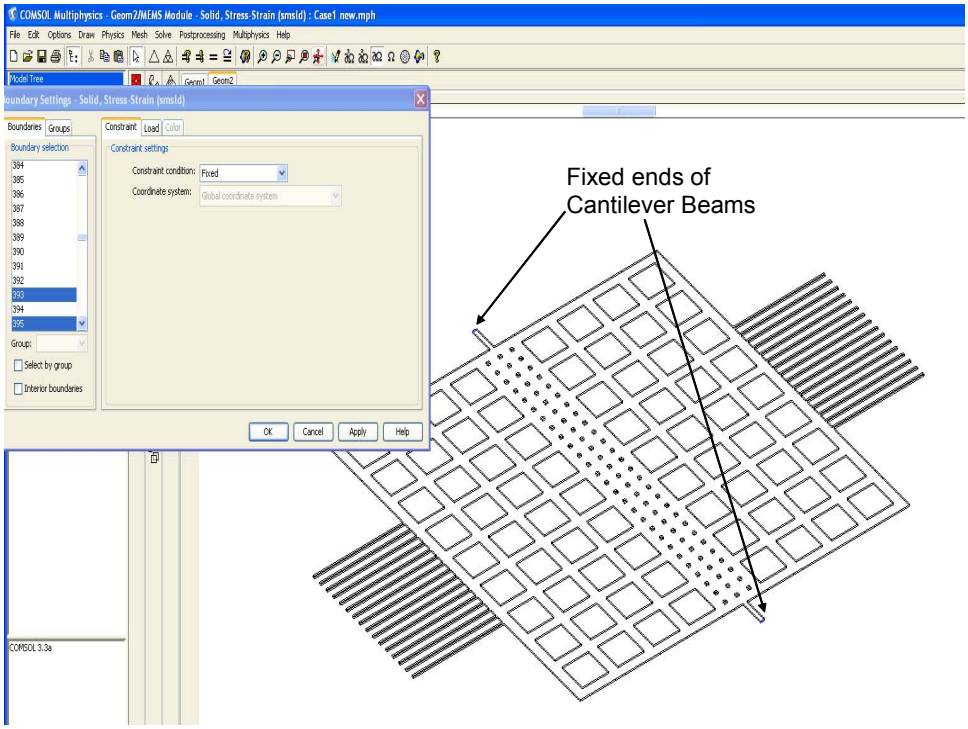

Figure 28. Primary device with fixed boundary conditions.

After setting the materials and boundary conditions, meshing the device was important. This at many times was the most difficult part. If it is meshed too

finely, then the solution consumes hundreds of megabytes of memory and the solution time increases linearly as the number of meshing is increased. However, if the computer system does not have enough RAM, the *COMSOL* program will resort to using virtual memory (hard drive storage) and in this case, the solution time can increase by one to three orders of magnitude. If it is meshed too coarsely, then the physical results are not as accurate. Therefore a large amount of time was spent trying to achieve a reasonable meshing, and in fact a solution that was mesh independent. In the case of simulating just the Eigen frequency modes, this was not as important an issue as it was in simulating the device actuation under a sound wave which will be discussed in Chapter VI. Figure 29 shows the primary device mesh with the normal mesh size chosen for this simulation. It should be apparent that the meshing is more detailed in the areas of small features or places where more detailed results were required.

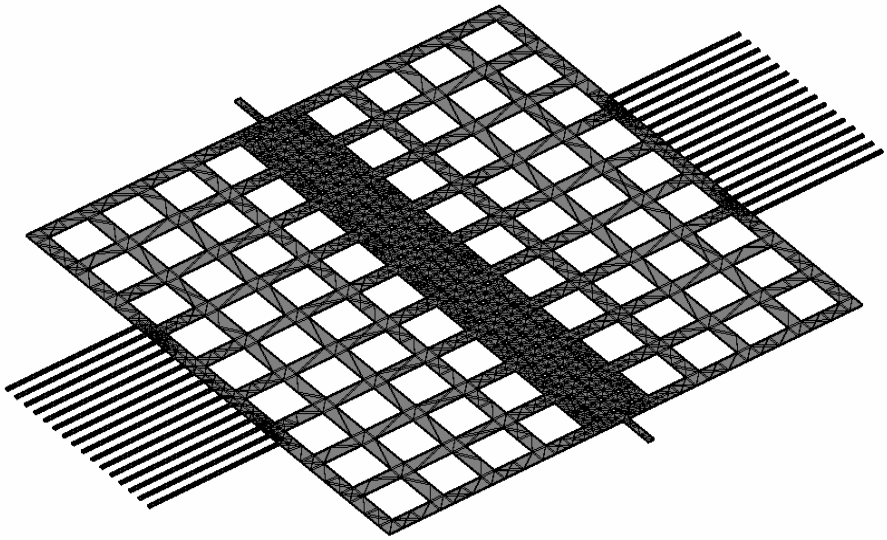

Figure 29. Normally meshed primary device.

Once the device is meshed then the solver parameters can be set. Since the structure in Figure 29 has two Eigen modes, the solver parameters were set to analysis → Eigenfrequency, solver → Eigenfrequency, and the desired number of Eigen frequencies were set to three (one extra for exploring higher order modes), as illustrated in Figure 30.

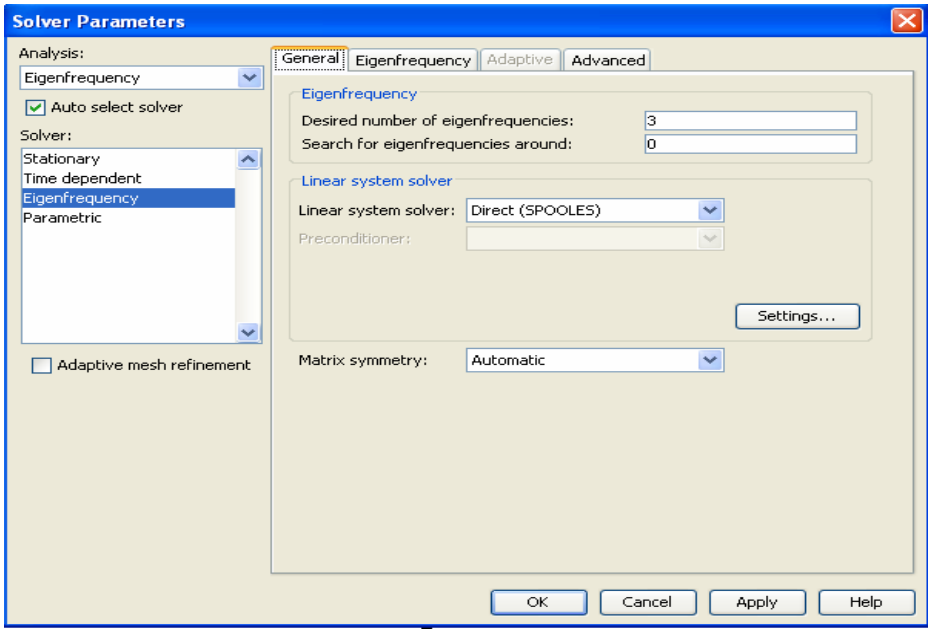

Figure 30. Solver parameters settings.

Finally the simulation is carried out to determine the Eigen frequencies. The amount of time that the simulation takes varied greatly depending on the device complexity that was simulated and the tightness of the meshing chosen.

1. Rocking and Bending Modes

As discussed in Chapter I, the rocking mode looks like a seesaw as it rocks back and forth, while the bending mode looks like a bird bending its wings or flapping its wings in flight. Figure 31 (a) and (b) show cartoon time sequenced representation of these two motions using the simulated data. Figure 32 shows the 3D view of the primary device in the rocking mode and Figure 33 shows the primary device in the bending mode.

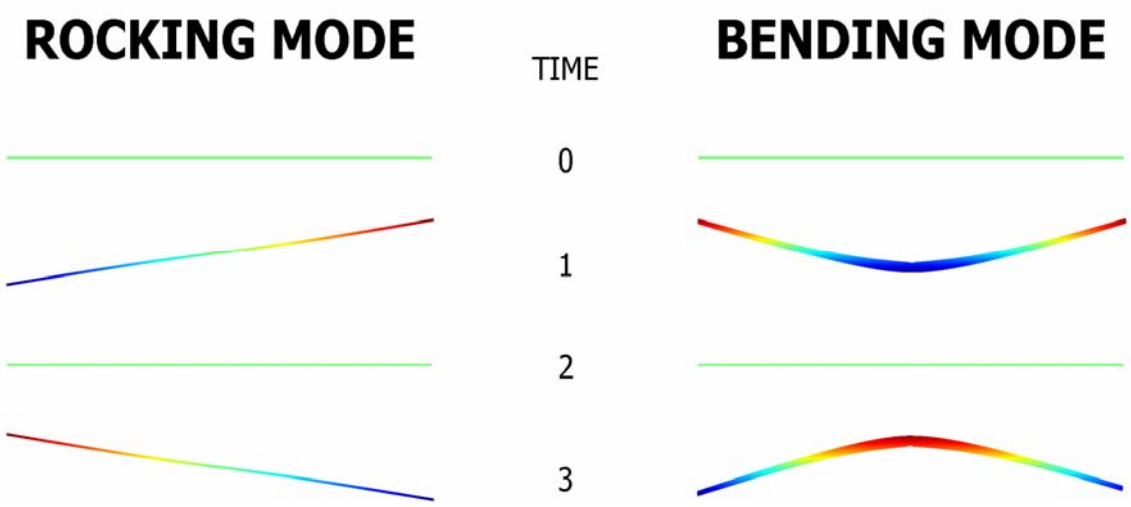

Figure 31. Time sequence of (a) rocking and (b) bending modes.

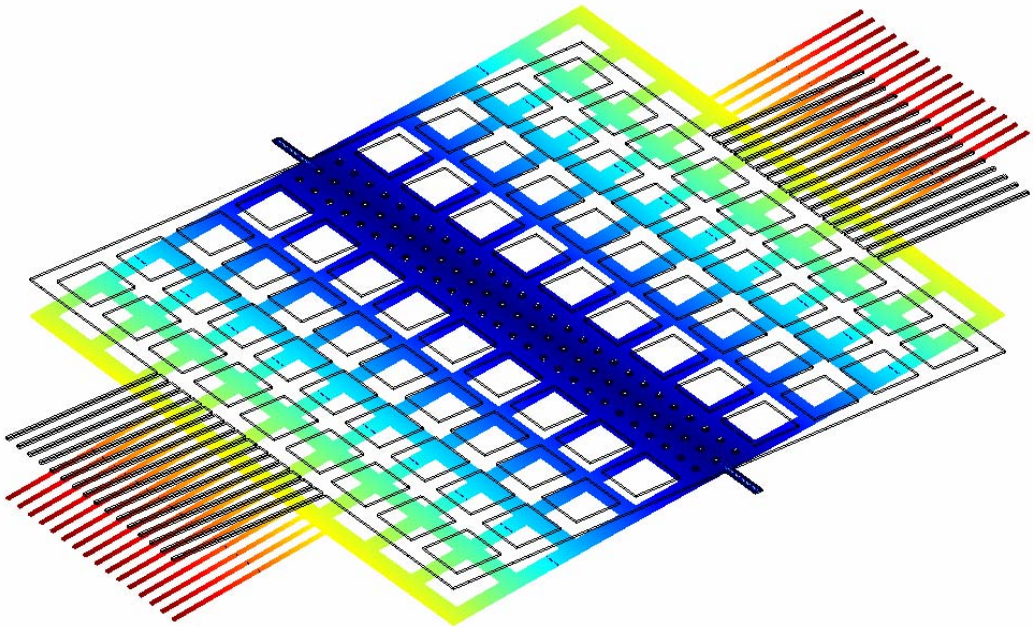

Figure 32. Primary device in rocking mode representing time 1 in Figure 30 (a).

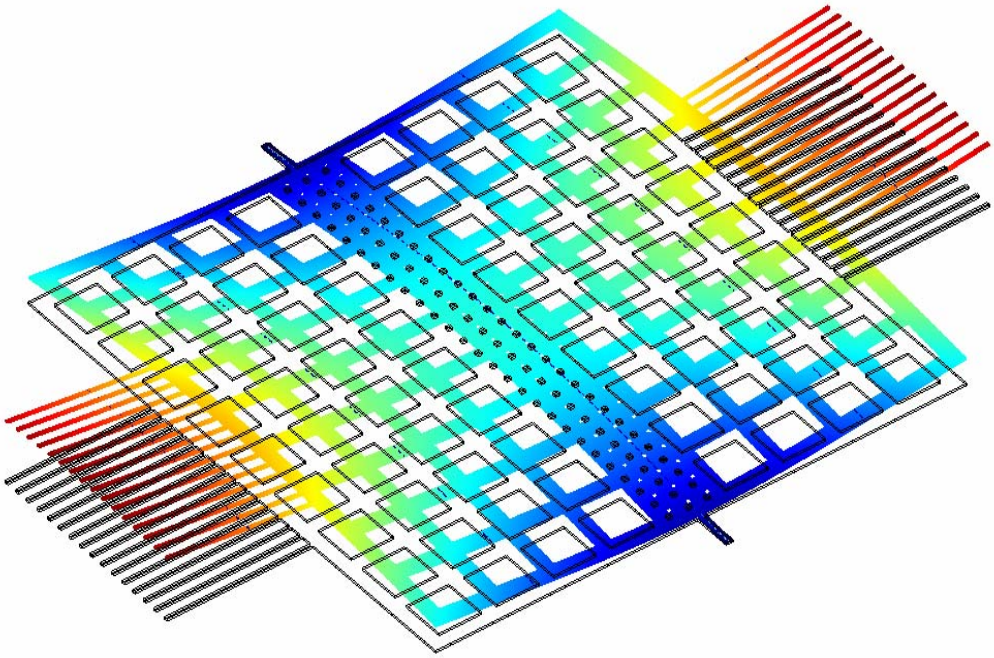

Figure 33. Primary device in bending mode representing time 1 in Figure 30 (b).

B. COMPARISON OF *ANSYS* AND *COMSOL* SIMULATION RESULTS

Table 2 shows the results for some of the 21 devices simulated in *ANSYS* and *COMSOL* side by side.

DEVICE			CANTILEVER BEAM		HOLES		ANSYS SIMULATED FREQUENCY*		COMSOL SIMULATED FREQUENCY	
Number	Length (μm)	Width (μm)	Length (μm)	Width (μm)	Number per wing (across x down)	Square hole Length (μm)	Rocking Mode (kHz)	Bending Mode (kHz)	Rocking Mode (kHz)	Bending Mode (kHz)
1	1080	1080	75	14	4 x 9	86	2.7	6.8	3.0	6.8
2	1080	1080	75	14	3 x 7	120	2.9	7.0	3.1	6.7
3	1080	1080	75	14	6 x 13	50	2.6	6.8	2.8	7.0
4	1080	1080	37.5	14	4 x 9	86	3.7	7.3	3.8	7.4
5	1080	1080	150	14	4 x 9	86	2.0	5.8	2.3	5.7
6	1080	1080	37.5	14	3 x 7	120	3.8	7.4	3.8	7.3
7	1080	1080	150	14	3 x 7	120	2.1	6.0	2.3	5.7
8	1080	1080	37.5	14	6 x 13	50	3.8	7.4	3.5	7.2
9	1080	1080	150	14	6 x 13	50	1.9	5.6	2.1	5.8
10	850	1080	75	14	3 x 9	86	3.8	7.9	4.0	7.7
11	850	1080	37.5	14	3 x 9	86	5.4	8.8	5.1	8.6
12	850	1080	150	14	3 x 9	86	2.7	6.5	3.0	6.3
13	1380	1080	75	14	4 x 7	120	2.1	5.2	2.3	5.3
14	780	1080	75	14	2 x 7	120	4.2	8.6	4.5	7.9
15	1540	1080	75	14	6 x 9	86	1.8	4.5	1.8	4.7
16	1550	1070	75	14	9 x 13	50	1.7	4.6	1.7	4.9
17	750	1070	75	14	4 x 13	50	4.2	8.3	4.3	8.2
18	1080	1080	75	14	4.5 x 9	86	2.7	6.2	2.9	6.4
19	610	610	75	14	2 x 5	86	6.1	15.1	6.3	14.8
20	1080	610	75	14	4 x 5	86	3.3	7.8	3.5	8.2
21	1540	610	75	14	6 x 5	86	2.1	4.4	2.2	4.8

*Simulated with Dr. Kim's ANSYS code

Table 2. *ANSYS* vs *COMSOL* simulations for the chip in Figure 27.

After simulation, testing became the next priority. The following chapter discusses the details of the lab setup and the testing conducted.

THIS PAGE INTENTIONALLY LEFT BLANK

IV. DEVICE TESTING

The directional sensors layout using MEMSCAP software (see Figure 27) was fabricated by the MEMSCAP foundry. Figure 34 shows an actual view of one of the sensors from an optical microscope. The grating structures at the edges of the wings are not clearly seen due to the low magnification of the microscope. However, the major features are clearly visible.

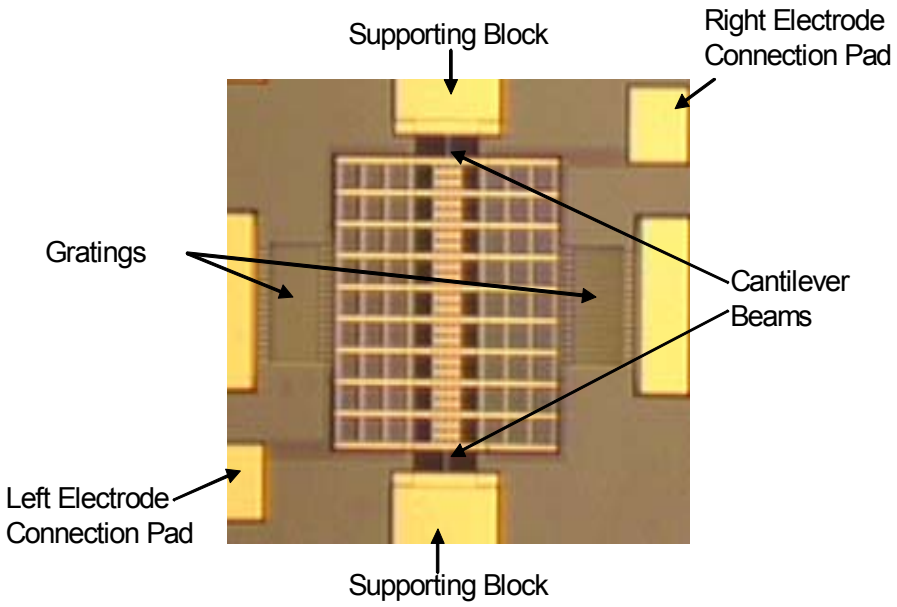

Figure 34. Optical microscope view of primary device. The wing structure is 1080 micrometers by 1080 micrometers.

A. WIRING AND PACKAGING

Using a *Kyocera* 68 Pin Grid Array Package, purchased from *Addison Engineering Inc.*, multiple chips were packaged and wired up for testing.

Wiring was conducted using a 4500 Digital Series, *Kulicke & Soffa*, Manual Wire Bonder machine. This machine solders and spools wire on the micrometer scale, while the operator controls placement via a microscope and control panel.

Figure 35 shows the device in its package and fully wired. In Figure 35, the chip package is placed in a retaining hoop to mitigate movement of the package; this was part of the testing rig that will be explained in more detail later in the chapter.

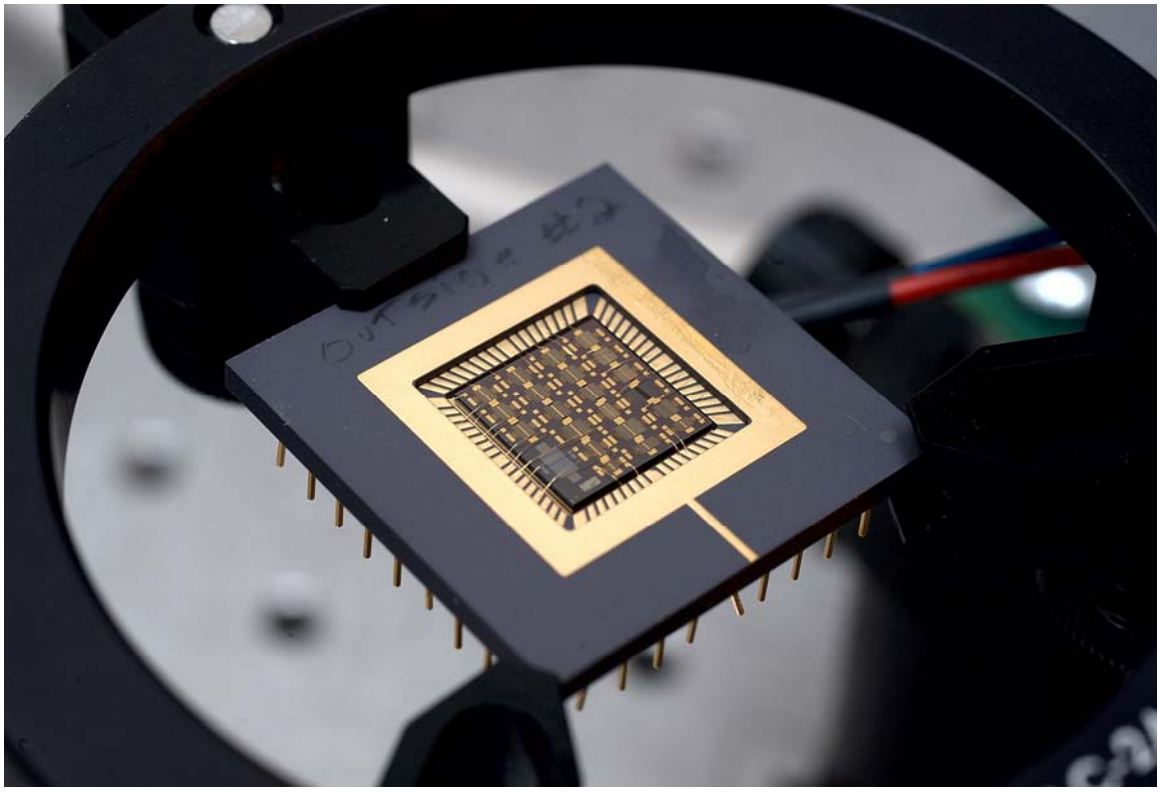

Figure 35. Chip in its package and wired.

Figures 36 and 37 show the schematics of the wiring used for connecting a set of sensors located in the outer and inner parts of the chip. Figure 38 shows the pin numbering. Pins 3, 8, 11, and 15 were used to supply the ground signal for sensors in Figure 36; where as, pins 7 and 11 were used as ground for the sensors in Figure 37. Separating the chip wiring into this configuration made it

easier to run wires as each wire is placed manually via the assistance of the machine. If all 21 designs were wired on one chip, then it would have been clustered with possibility of shorting some of the wires.

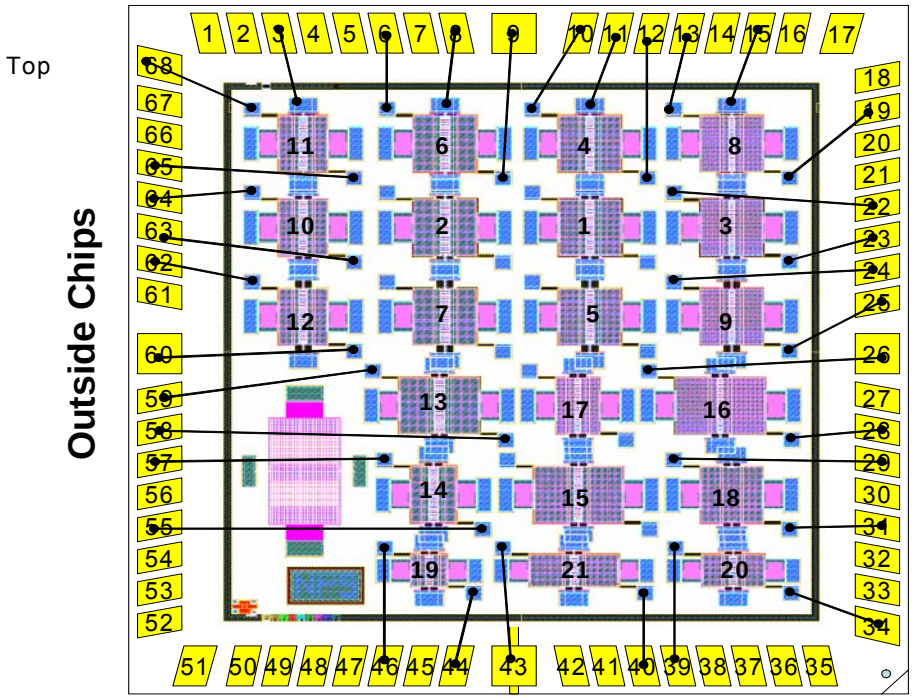

Figure 36. Outer devices wiring diagram.

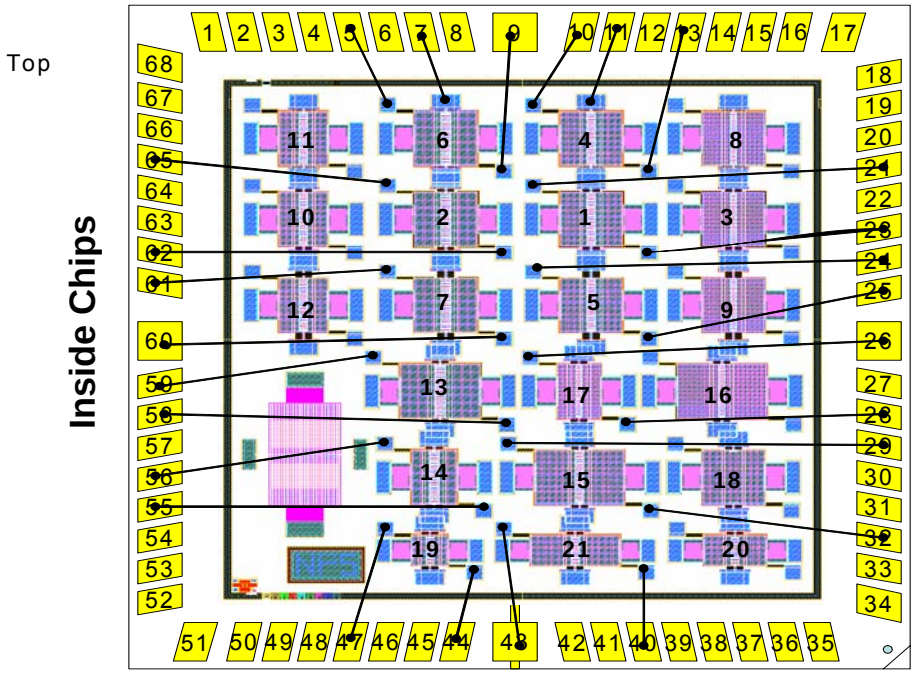

Figure 37. Inner devices wiring diagram.

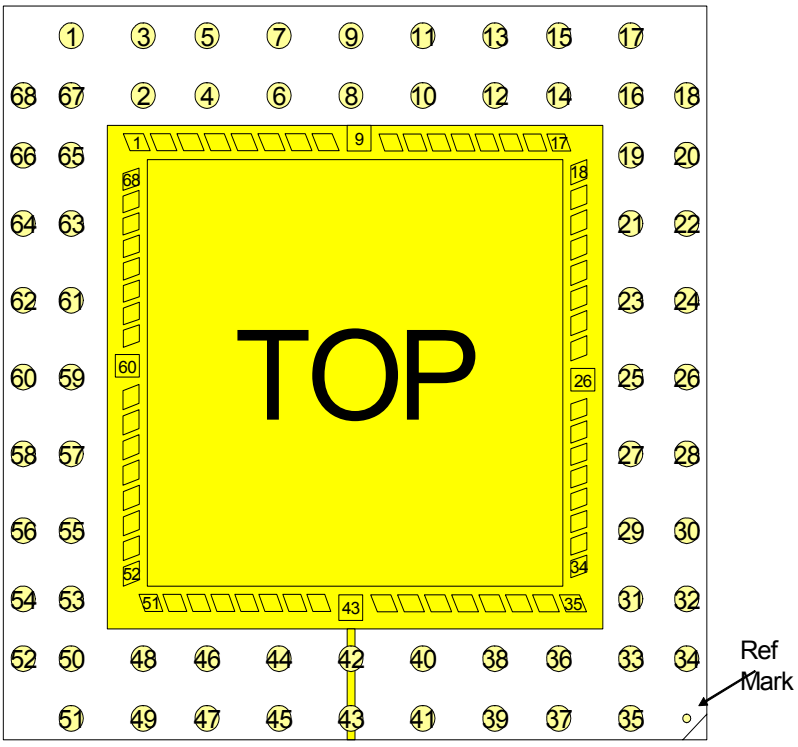

Figure 38. Pin numbering diagram. Pins are on the back. Numbered as if seen from the front. Numbers correspond to its same number pad.

B. EXPERIMENTAL SETUP

Figure 39 shows a picture of the laboratory setup used to measure the vibrational amplitudes of the sensors. Each of the 21 devices is to be tested, both electrostatically and via sound actuation, in order to test for their performance.

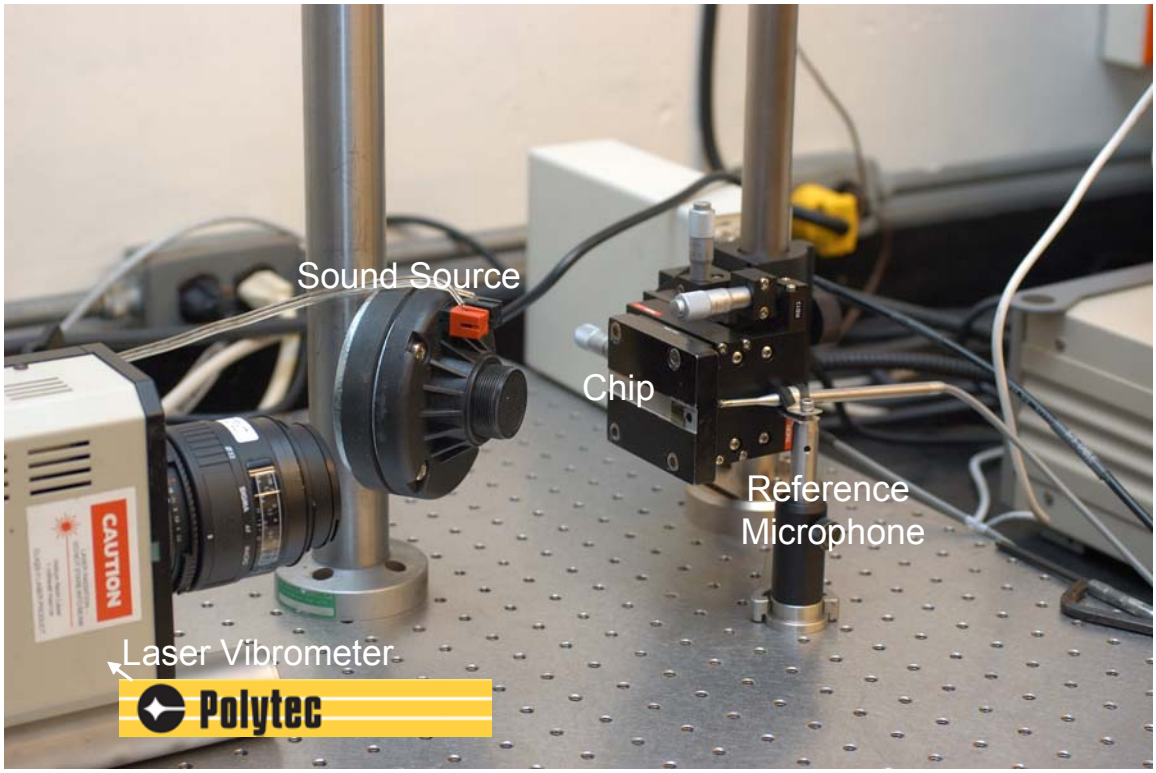

Figure 39. Equipment in lab setup used for measuring vibrational amplitudes.

1. Functions of Equipment Used

As Figure 39 shows, there were some key components integral to the testing of each device. They were the reference microphone, the sound source, the laser vibrometer, and the chip being tested. Some additional equipment was used and will be discussed as appropriate.

The reference microphone was placed close to the sensor chip to measure the sound pressure. It is a *Bruel & Kjaer* Pressure-field 1/8" Microphone type 4138. It has a relatively flat response curve from 20 Hz to 20 kHz with 0.939 mV/Pa sensitivity.

The sound source was a *Selenium* loudspeaker type DH200E attached to a *Hewlett Packard* (HP) 3314A Function Generator and HP 467A Power Amplifier. The purpose of this equipment was to produce a set amplitude and frequency of the incident sound wave. Incident sound wave angle was adjusted manually by adjusting the speaker position.

The laser vibrometer was a *Polytec* single point vibrometer model OFV 302, with a model OFV 2600 controller. Its purpose was to measure the displacement of the wings, to a resolution in the sub nanometer range.

Additional equipment not shown in Figure 39, but just as valuable was a lock-in amplifier and an oscilloscope. The lock-in amplifier was and *EG&G Princeton Applied Research* model 5210. Lock-in amplifiers are used to measure the amplitude and phase of repetitive AC signals buried in noise. The oscilloscope was a four channel *Agilent Infiniium* DSO8064A model. It was used to show the signal from the reference microphone and the device being tested on the same screen.

C. ELECTROSTATIC TESTING

Prior to Naval Postgraduate School receiving their own laser vibrometer, *Teledyne Technologies, Inc. (*formerly *Rockwell Scientific)* in Thousand Oaks, CA, allowed the project team to use their laser vibrometer.

Testing was conducted at their facility in Thousand Oaks, and therefore needed to be limited in the number of devices tested. The devices chosen to test were 4, 5, 8, 14 and 19 as indicated in Figure 37. Each device was

electrostatically actuated at a voltage of one volt over a frequency sweep from zero to 20 kHz. Note that for actuating the rocking mode the bias should be applied to only one side of the membrane.

Testing started with device 4 because it was easy to access and easiest to manually wire the pins to the electrostatic source. In addition device 4 was similar to the primary device except it had a smaller cantilever beam size. Results from device 4 did not show two resonant frequency amplitude peaks as were expected. Results are shown in Figure 40; note that the Y axis is velocity amplitude. Remember, the bending mode was predicted to be at approximately 7.5 kHz for this device, which is close to the measured value in Figure 40. However, no rocking mode was seen on the graph. The peak near 20 kHz is a higher order mode.

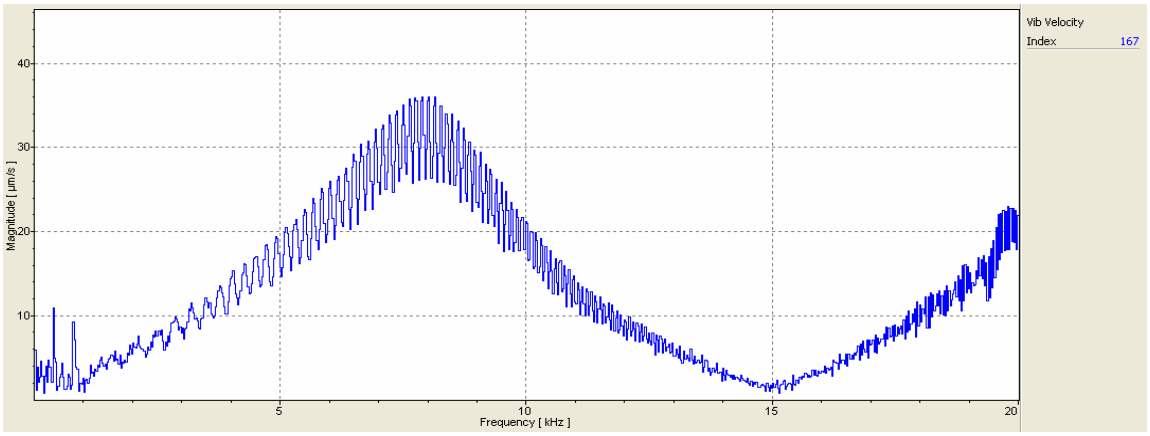

Figure 40. Device 4, magnitude of velocity versus frequency curve.

This was perplexing, and because of this result, device 8 was selected to be tested next. It was assumed that perhaps the missing rocking mode was due to the damping which broadens the peak reducing the amplitude.

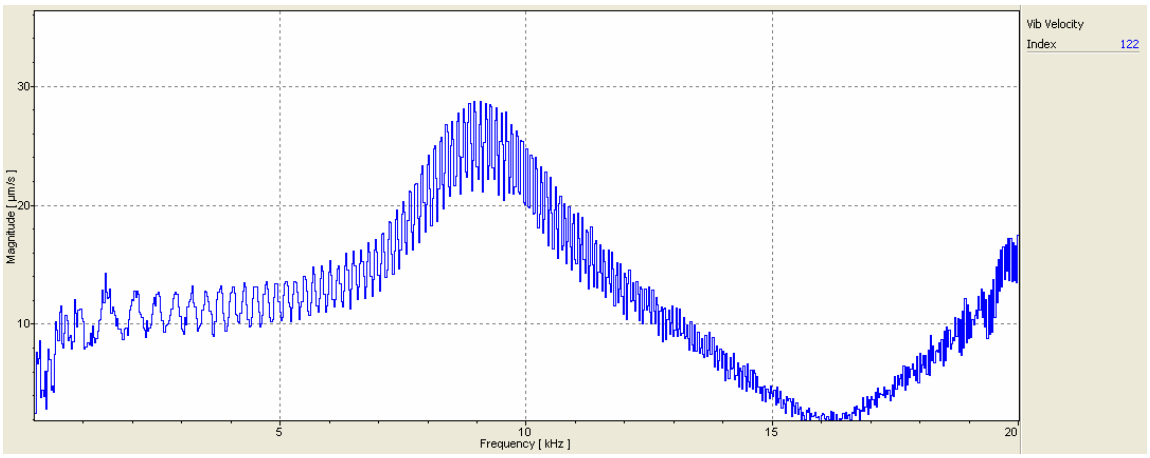

Figure 41. Device 8, magnitude of velocity versus frequency curve.

Device 8 was the same dimensions as device 4, in length and width of the wings, and also in cantilever beam size; the differences were the hole size and number of holes. Device 8 did not show the desired rocking mode either, as shown in Figure 41.

Continuing to be perplexed, the affects of the cantilever beam length were probed next by selecting device number 5 as the next device to be tested. Again, results were not as expected. The longer cantilever beam did not help the rocking mode to appear.

At this point, it was decided to test a device with smaller wing dimensions. Remember that the rocking mode frequency was inversely proportional to mass (equation 1.20). The prevailing thought was that a smaller device would have a higher rocking frequency and therefore might allow the rocking mode to be seen more clearly. Following this train of thought device 14 was chosen next. Device 14 did not show the desired results either, but device 14 was only smaller in length.

Finally, device 19 which had the smallest wing dimensions was tested. Device 19 provided the frequency response curve that was expected. Figure 42 clearly shows the rocking and bending mode amplitude peaks as expected.

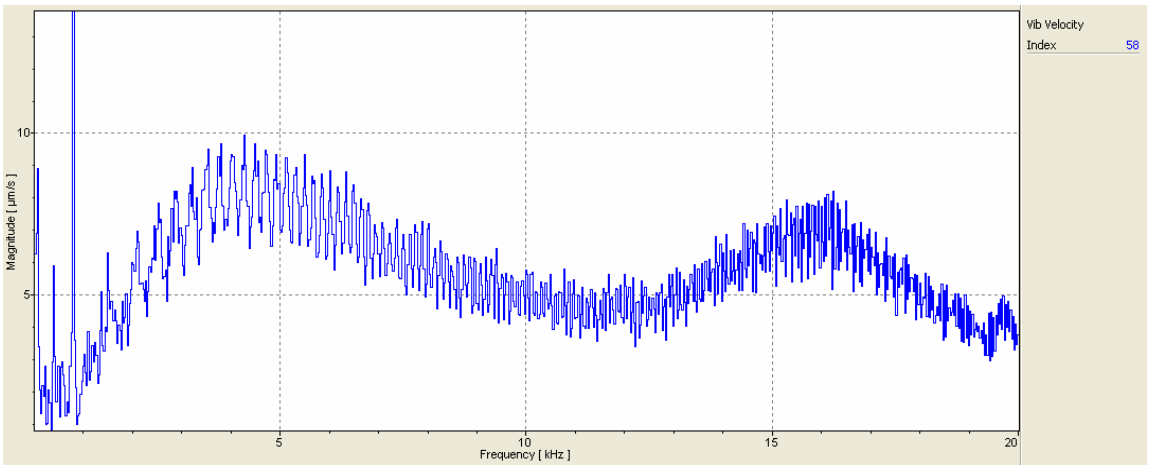

Figure 42. Device 19, magnitude of velocity versus frequency curve.

If the results are converted to displacement amplitude vice velocity amplitude (displacement = velocity/ω) , the results are 4.75 kHz and 15.1 kHz. Remember, from Table 2, the expected rocking mode was approximately at 6.0 kHz and the bending mode was expected at approximately 15 kHz. However, these results of approximately 4.75 kHz and 15.1 kHz were within reason and promising. Explanation as to the differences between simulation and testing is discussed in Chapter V.

1. Visual Results

Besides the frequency response curves shown earlier, the laser vibrometer computer program that accompanied the controller allowed the operator to superimpose an optical image over an animation of the actual device amplitude data. An animation can easily be created during this process. Figure 43 shows the rocking mode of device 19 at 4.75 kHz in this manner. Figure 43 is shown in three screen shots side by side, as the device rocks from the left side down to the right side down. Similarly, Figure 44 shows the bending mode at 15.1 kHz as well. These figures are a graphical representation of the actual data.

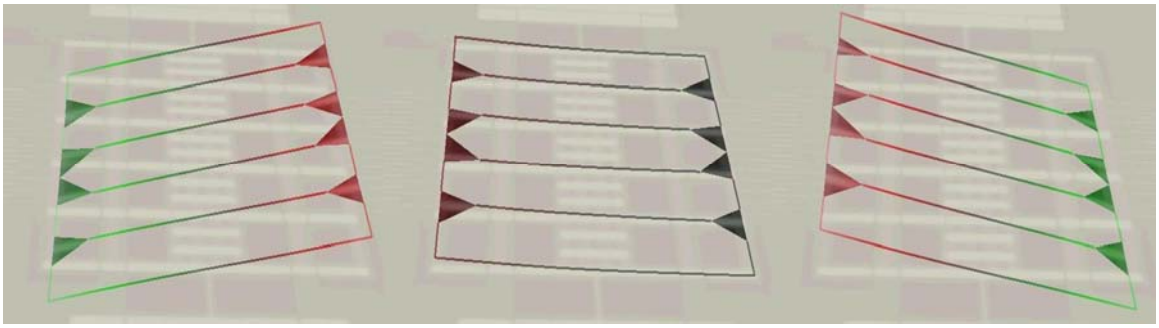

Figure 43. Device 19 electrostatically driven rocking mode.

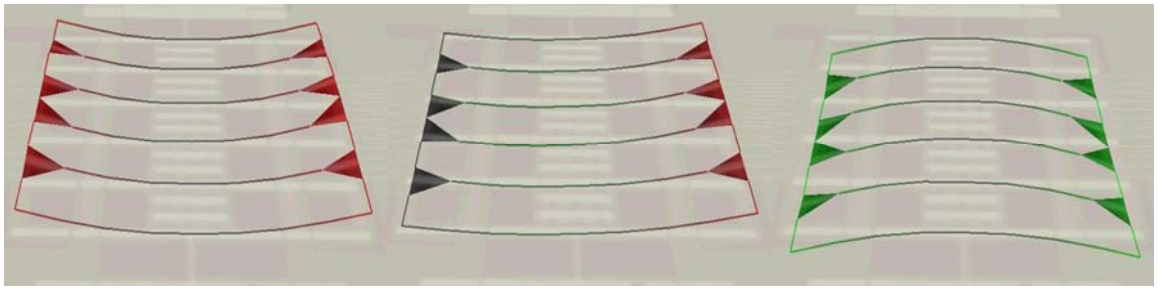

Figure 44. Device 19 electrostatically driven bending mode.

Figure 45 shows a detailed image of device 19 at one instance of time while it is undergoing a rocking mode. The number of data points taken by the laser on the gratings was minimal to save in computation time, thus some noise is seen in the figure; however, the extreme detail was useful in some instances.

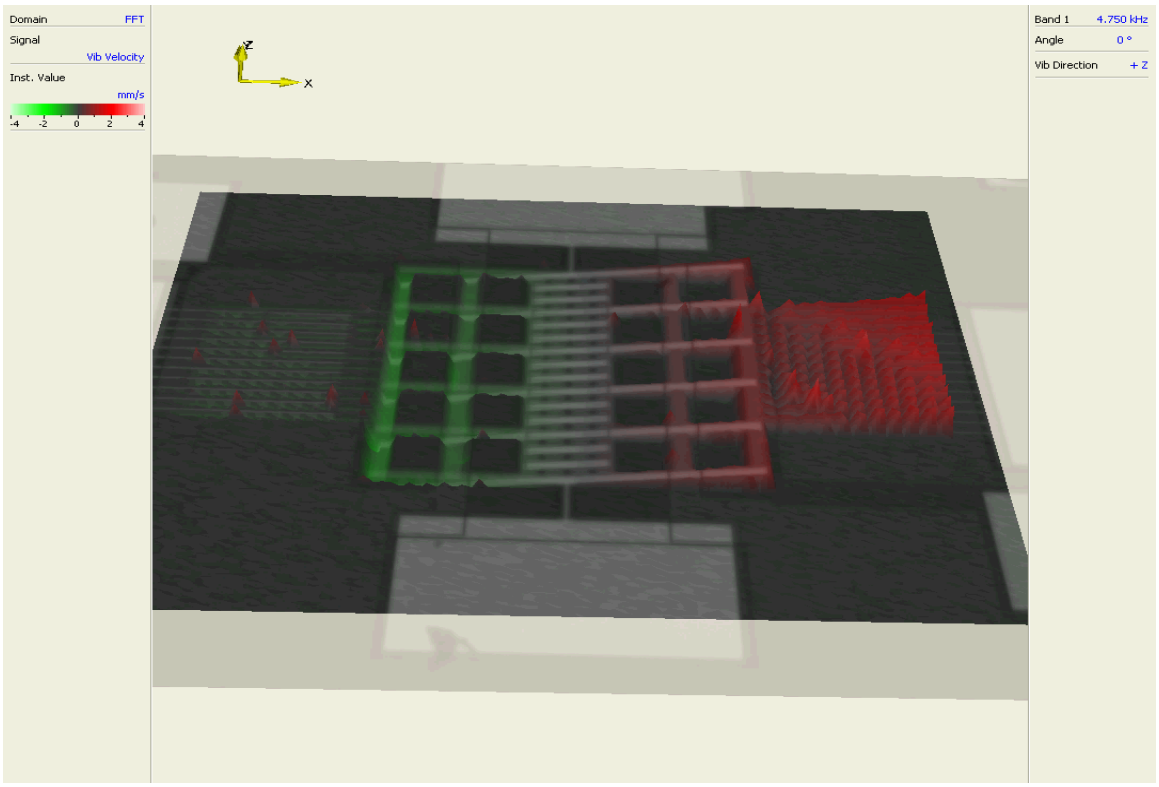

Figure 45. Device 19 electrostatically driven, at 4.75 kHz, rocking mode detailed view.

2. Computer Controlled Evaluation Board with M3110 Capacitance Measurement Chip

Early on in the electrostatic testing phase, it became apparent the Dr. Kim's optical method of measuring displacement would not work well with these PolyMUMPs devices. It turns out that due to the length of the gratings and the manufacturing process that there is residual stress in the gratings that cause the gratings to bend slightly upward. The net result of this bend is that the optical laser system discussed in Chapter II and shown in Figure 27, did not allow the diffraction pattern to accurately determine displacement. A different system needed to be employed.

Many MEMS devices in industry use the capacitive approach to measuring displacement and a commercial board was readily available to achieve the accuracy required for this device. The stated sensitivity of the board

is approximately four aF/(Hz)$^{1/2}$, remarkably sensitive [www.irvine-sensors.com]. In addition each of the techniques used on this board could eventually be miniaturized and easily placed on the same chip as the biomimetic sound device being tested.

Figure 46 shows the *Irvine Sensors*, MS3110BDPC board attached to a chip about to be tested electrostatically; the electrostatic connections have not yet been made though.

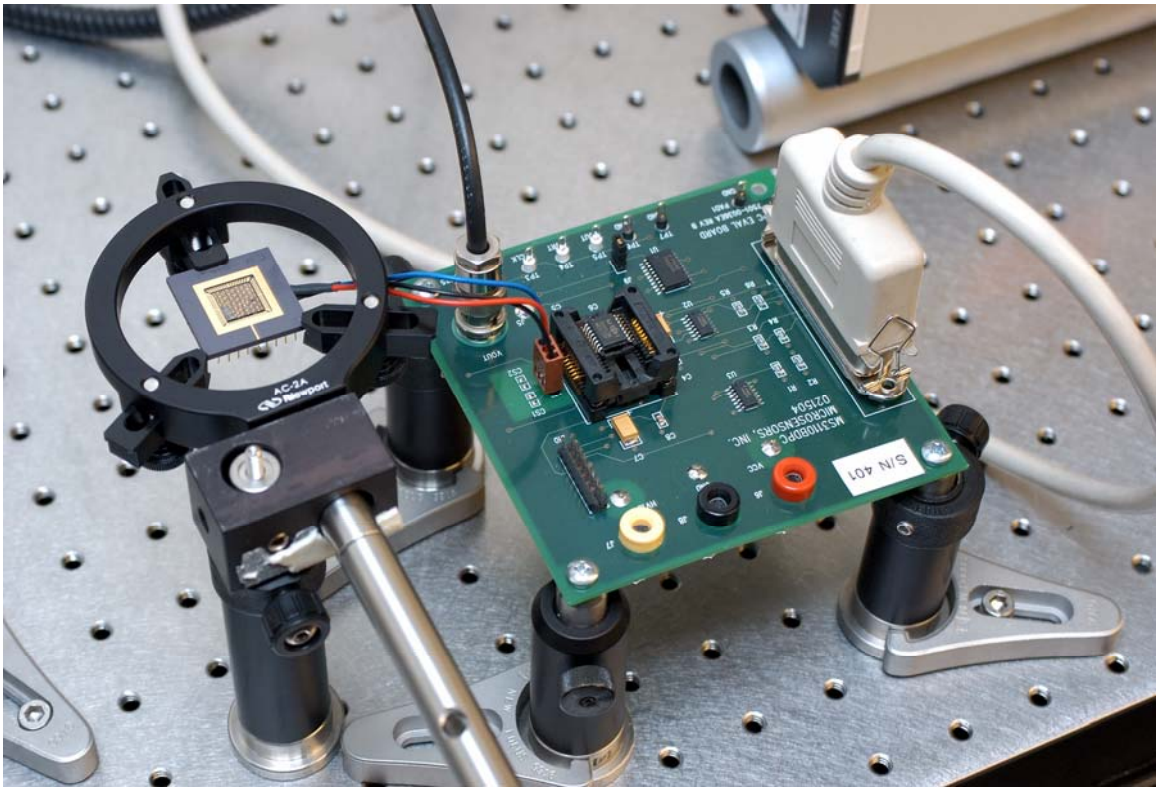

Figure 46. Computer controlled evaluation board with M3110 capacitance measurement chip.

D. SOUND TESTING

Once the concept of rocking modes and bending modes of the actual biomimetic devices were proven with electrostatics, it was imperative to test the devices in a sound field.

1. Polytec Laser Vibrometer

The Naval Postgraduate School received its *Polytec* single point vibrometer model OFV 302, with a model OFV 2600 controller and the lab was setup as shown previously in Figure 39. The focus was on device 19 since this device showed both a clear rocking and bending mode during electrostatic testing and the most data was available for validation of the results. The sound pressure at the device was about 1 Pascal (approximately 95 dB).

2. Results

Figure 47 shows the response of device 19 when actuated using a sound wave. It is showing the bending mode at 15.1 kHz; again it is three screenshots side by side to portray a time sequence. Displacement was found to be less than one nanometer primarily due to leaking of the sound pressure through the holes used to control the damping. The rocking mode amplitude was too small to be measured since it depends on the pressure difference between the two wings. A detailed explanation is given in Chapter V explaining this behavior.

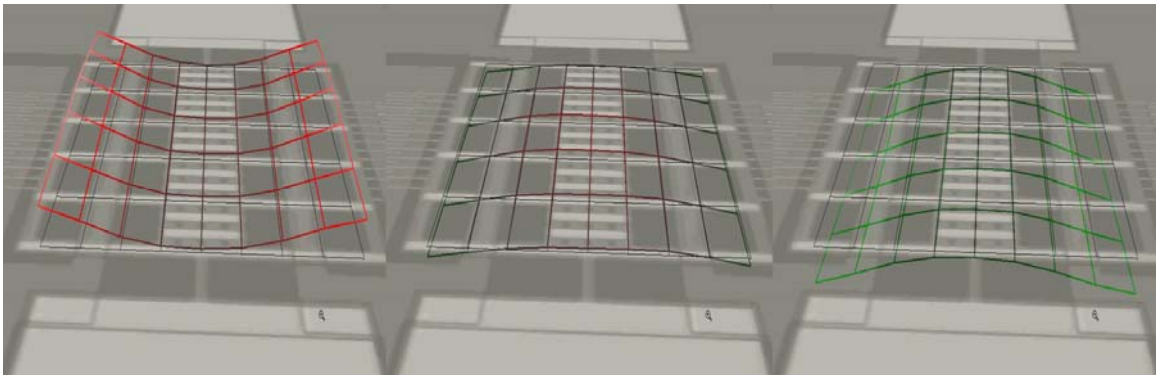

Figure 47. Actuation of device 19 using sound incident normal to the membrane surface. The bending mode can be clearly seen from the time series.

E. ADDITIONAL INFORMATION OBTAINED FROM FREQUENCY RESPONSE CURVES

Figure 48 shows the frequency response curve from one of the testing runs on device 19. It clearly shows a rocking mode peak and a bending mode peak. Additional information, though, can be gained from such graphs. The full-width-at-half maximum of the resonance peak (normal mode) can be used to determine the quality factor (Q). Q is defined as the ratio of resonance curve width at half maximum to the peak resonance frequency (ω_o). The full-width-at-half maximum (FWHM) is approximately equal to two times the damping constant (β) [Taylor, 2005]. That means the Q value is a qualitative measurement and is inversely proportional to the damping constant, as seen in equation 1.34 [Kinsler *et al*., 2000].

$$Q = \omega_o / 2\beta \tag{1.34}$$

Therefore by looking at the frequency response curves, a clear indication of the damping can be seen. The wider the resonance curves at the half maximum points, the stronger the damping. Additionally, the damping coefficient can be calculated within some minor margin of error, directly off the response curves and thus evaluated device changes more rapidly.

Equation 1.34 assumes that the amplitude of the resonance peak is power amplitude; however, the laser vibrometer output is velocity amplitude as shown in Figure 48. Therefore, a formula that utilized the velocity amplitude was derived. Since full-width-at-half maximum (FWHM) applies to power which is proportional to amplitude squared, full-width-square root of 2-maximum [$FW\sqrt{2}M$] applies here. Derivation is shown in Appendix C, but the final result is equation 1.35.

$$FW\sqrt{2}M \approx 2\beta \tag{1.35}$$

Sometimes it is easier to measure the full-width at half-maximum, and therefore using a similar derivation it can be shown that FWHM = $\sqrt{3} * 2\beta$.

The damping parameter can be estimated using either approach. Then a comparison of the damping constant to that of the modal frequency peak is compared using the relationships listed as equation 1.36 [Taylor, 2005].

$$\begin{aligned} \beta < \omega_o &\Rightarrow under\ damped \\ \beta = \omega_o &\Rightarrow critically\ damped \\ \beta > \omega_o &\Rightarrow over\ damped \end{aligned} \qquad (1.36)$$

A comparison of the damping constant to that of the rocking mode frequency for device 19 using the data shown in Figure 48 was conducted and the result is that device 19, with its large holes, is slightly under damped; $17969\frac{rad}{\sec} < 27017\frac{rad}{\sec} \Rightarrow \beta < \omega_o \Rightarrow$ under damped. Keep in mind that there is only a two micrometer air gap under the wing structure and most of that air needs to move through the relatively large holes in order for an appreciable displacement to occur, thus slightly under damped makes sense.

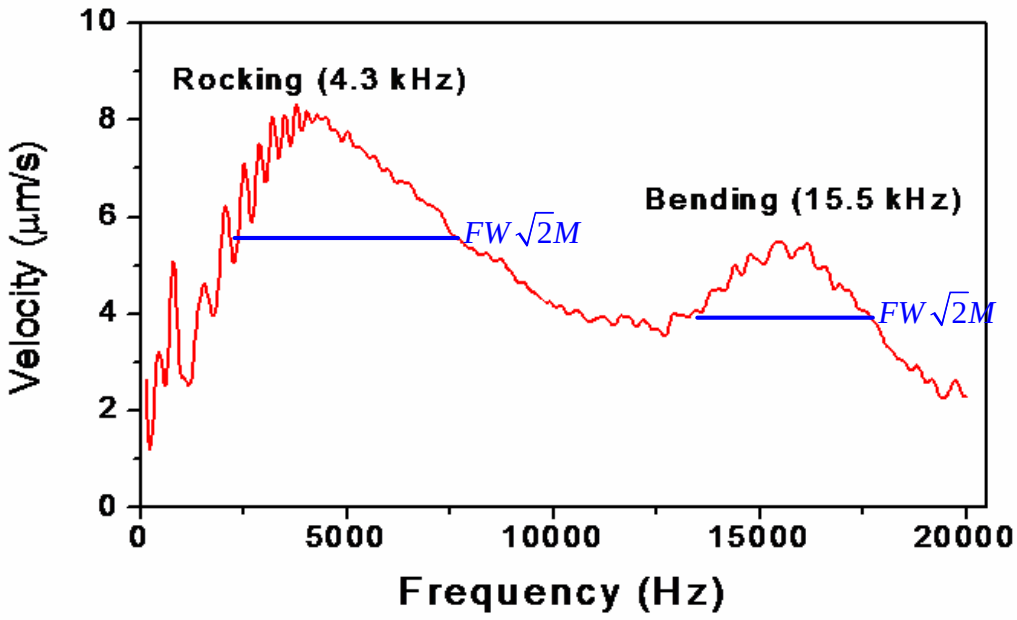

Figure 48. Velocity as a function of excitation frequency for device 19.

THIS PAGE INTENTIONALLY LEFT BLANK

V. POSSIBLE REASONS FOR DIFFERENCES BETWEEN SIMULATIONS AND EXPERIMENTAL RESULTS

The first question that comes to mind after seeing the testing results is why did the simulation predict a rocking mode at approximately 6 kHz and the testing result in a rocking mode of 4.75 kHz? The bending mode seemed to be almost right on, as the simulation predicted approximately 15 kHz and the testing showed 15.1 kHz. What could cause the differences?

A. TOLERANCES IN STRUCTURE SIZE

The first insight came while reviewing the optical microscope images more closely. It seems that the tolerances in the fabrication process allowed for minute changes to the dimensions of the devices.

Figure 49 shows an optical microscope view of device 19 with measurements of the some of the key dimensions that control the rocking frequency.

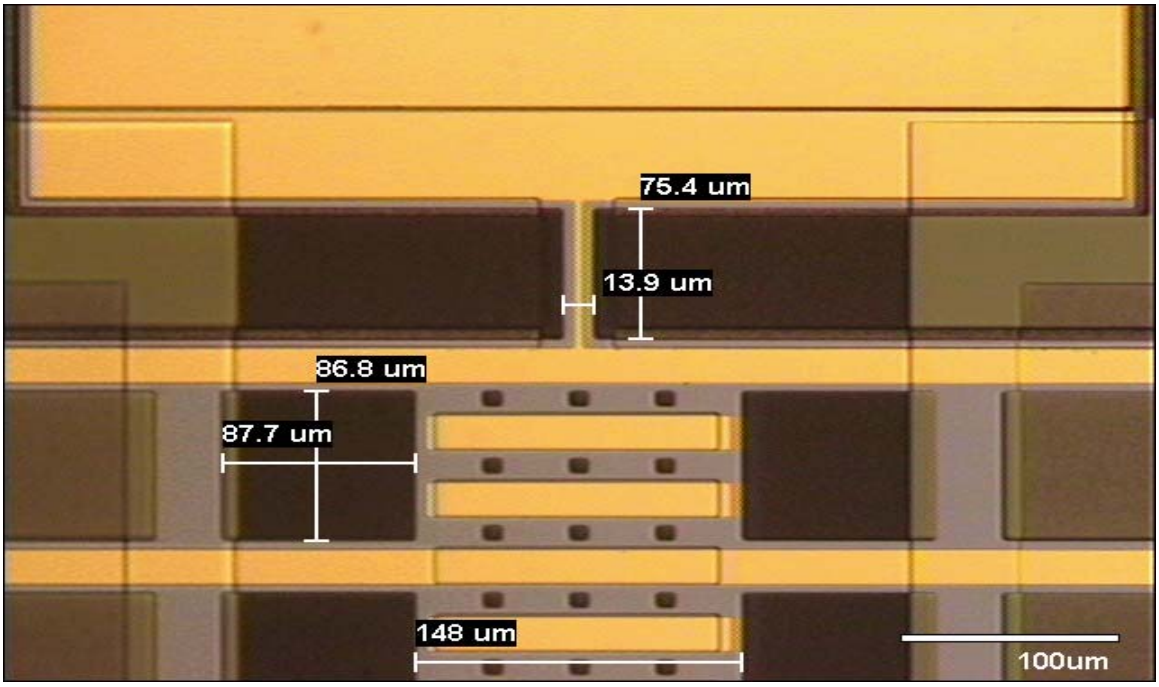

Figure 49. Device 19 optical microscope view with measurements.

Remember, from Table 2, the torsion beam was simulated to be 75 micrometers long and 14 micrometers wide. Figure 49 clearly shows that the cantilever beam on the actual device tested was 0.4 micrometers longer and 0.1 shorter in width.

B. SIMULATION SIMPLIFICATIONS

In addition to variation of the torsion beam dimensions, the gold layer on the polysilicon was not incorporated in the earlier simulation. Recall, equations 1.20 and 1.21 showed that the modal frequencies were inversely proportional to the mass of the device. Not including the gold might significantly affect the mass. So in order to incorporate the effects of the gold layer, additional simulations in *COMSOL* were conducted. The result is the rocking mode was lowered to 4.9 kHz which is much closer to the 4.75 kHz achieved during testing.

1. Revised *COMSOL* Simulation Results

Figure 50 shows the rocking mode modal frequency at 4.9 kHz. If Figure 49 is compared to Figure 50, the gold strips stand out more.

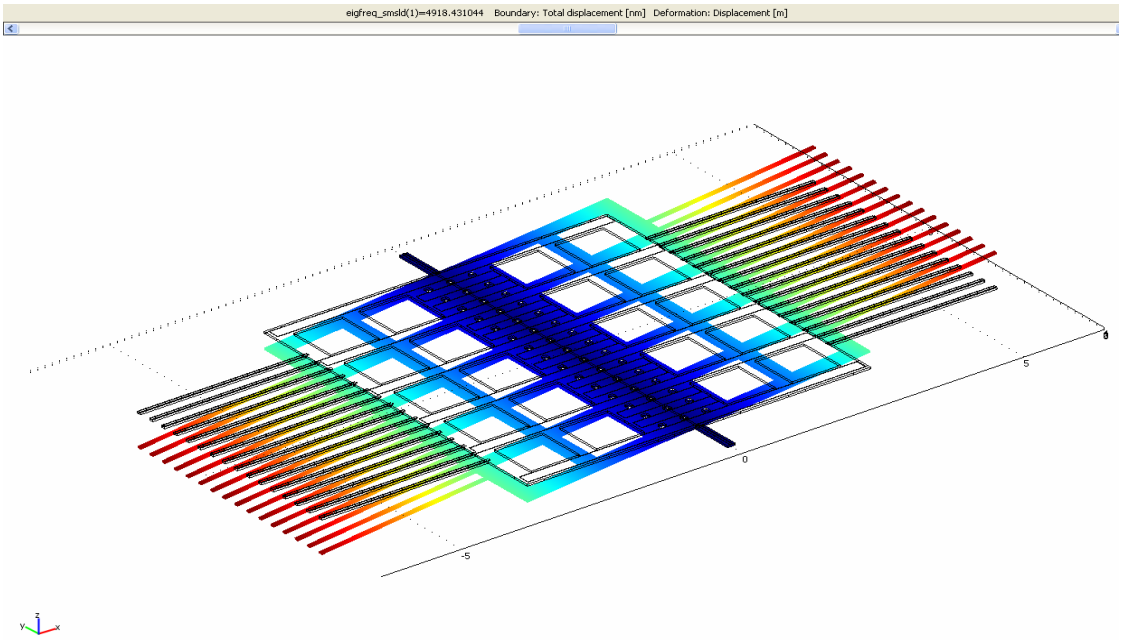

Figure 50. Device 19 *COMSOL* simulation with gold layer.

C. HOLE SIZE TOO LARGE CAUSING SOUND LEAKAGE

As was mentioned in Chapter IV, displacement of device 19 when subjected to an incident sound field was minimal at less than one nanometer. This was perplexing. Simulations had shown that displacement at the rocking modal frequency should have been in the tens of nanometers at the smallest. True these simulations were not simulations of the device subjected to a sound field, but it was believed that if the modal frequency was reached, displacement amplitudes should have been comparable. So why is it that the displacement was so low?

During the design phase, it was believed that as long as the damping holes were smaller than the wavelength of the driving sound that the holes would be negligible and the device would operate similar to that of a radar dome. In the radar dome, the holes, do not affect the electromagnetic properties of the dome.

The key physics mistake made here is that electromagnetic waves are transverse which actively interacts with the meshed surface of the radar system; whereas sound waves are longitudinal and pass through the holes which reduce the pressure difference required for driving the wing membrane. Therefore with too large of holes in the membrane, it is very easy for the pressures on either side of the membrane to nearly equalize; thus minimizing displacement.

1. Solid Plate Membrane

Simulations were conducted for a device with wing sizes comparable to that of device 19, but without the holes. Device 19 is 610 micrometers square which equates to 372,100 square-micrometers in area.

This solid plate device was simulated in a sound field of amplitude 1 Pa, at approximately 8.5 kHz. Displacement was approximately 70 nanometers for the rocking mode as shown in Figure 51.

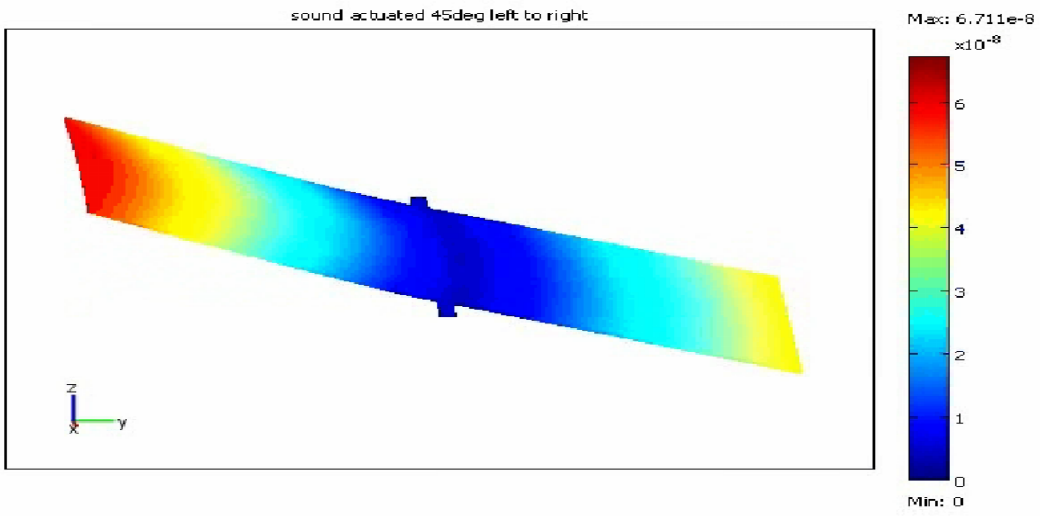

Figure 51. Solid Plate, sound actuated 45 degrees left to right, *COMSOL* simulation screen shot.

2. Affect of Holes in the Membrane

Now that it was known that a solid plate achieves a reasonable displacement, it was decided to study exactly what affect holes had on the overall displacement of the device 19. Figure 52 shows the displacement of the wings for device 19 under the same sounds field used for simulation of the solid plate in Figure 51. The maximum displacement in this case was found to be less than a nanometer compared to the almost 70 nanometers for the solid structure. The measured velocity (v) data for device 19 gave about 8 micrometers/sec at the peak of the resonance for rocking mode. Since the velocity and displacement (x) amplitudes are related by $v = \omega x$, the estimated displacement amplitude using the measured velocity data for the rocking mode is about 0.3 nanometers. This is the same order of magnitude as the simulated value considering the fact that the simulation gives an over estimation due to the exclusion of the damping effect. The Table 3 summarizes the simulated and experimental displacement amplitudes for device 19 along with that of the solid structure. The reason for the

difference in the resonance frequencies is that the simulated device does not contain the grating fingers, as the do not affect the displacement, and only added additional calculation time and memory to the simulation.

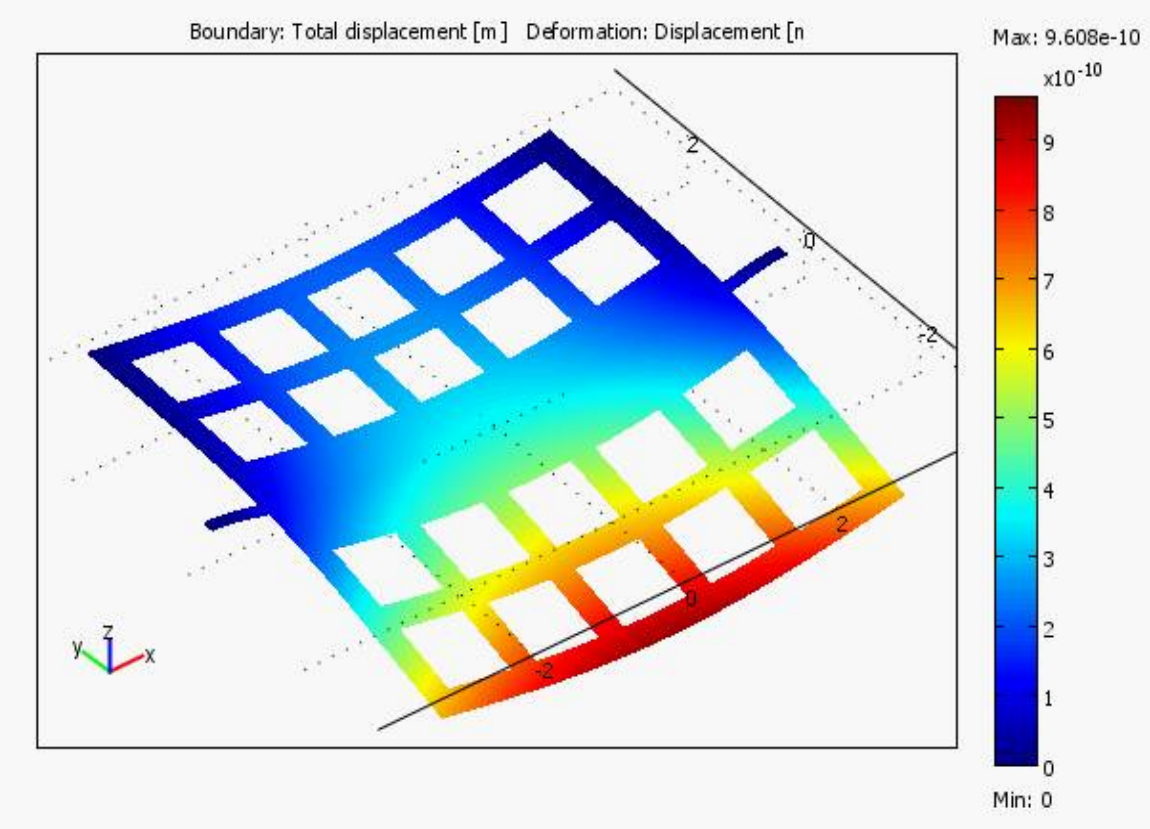

Figure 52. *COMSOL* simulation screen shot of the device 19 under the same sound field as the solid plate in Figure 51.

	Resonance Frequency	Area Removed	Device Displacement
Solid Plate 372,100(μm^2) 610 μm x 610 μm	8,490 Hz	none	67 nm
Simulated device 19 (without the grating fingers)	11,167 Hz (without the grating, lower mass => higher resonance frequency)	147,920 μm^2 (20 holes each 86 μm x 86 μm)	0.9 nm
Measured device 19	4.75 Hz	Same as above	0.3 nm

Table 3. Comparison of simulated and experimental displacements.

D. INCORPORATION OF SQUEEZE FILM DAMPING INTO THE SIMULATIONS

Squeeze film damping is a type of damping that occurs when a thin volume of a gas exists under a moving plate. As the plate moves down it needs to displace the air underneath; damping comes from the rate at which the plat can displace this gas. The damping reduces the vibration amplitude and broadens the resonance peak. This is the primary reason the simulation did not match the experimental data since the squeeze-film damping was not included in early simulations. Around the time that the discrepancy between the simulation and experimental data was discovered, *COMSOL* released its version 3.3a version. Built into this version was the ability to simulate squeeze-film damping in a way that did not appreciably increase the memory needs or the simulation time.

1. *COMSOL* Process

Section 7, of the *COMSOL* "MEMS MODULE" manual, discusses the details of the theory, but it is based on a modified Reynolds equation [*COMSOL*, 2006]. This whole process, although not *COMSOL* specific, is also described in the Veijola *et al.* 2005 paper. Figure 53 (a) shows visually that the air is being forced out from under the plate and escapes through the perforated holes in the plate. Figure 54 shows the equations that *COMSOL* is using in its film damping physics boundary condition section; Figure 54 also shows many of the settings used for simulations for the regions defined as holes. The regions defined as not holes, have its relative diffusivity (D_h) set to 1, its relative compressibility (C_h) and its Perforation admittance (Y_h) set to zero as shown in Figure 55. Figure 53 (b) shows graphically what the settings should be and why.

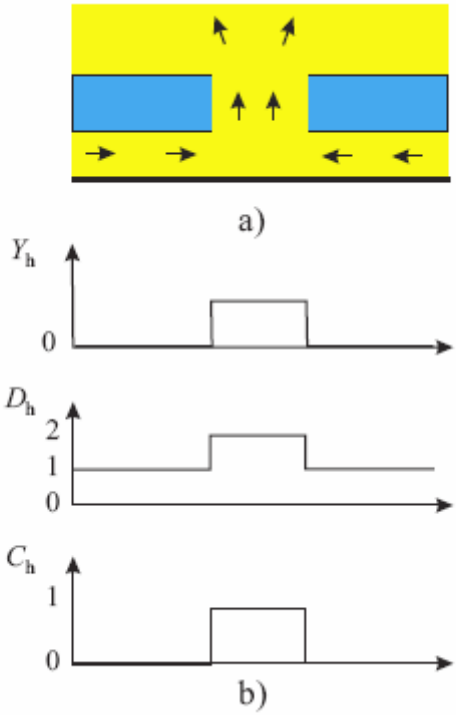

Figure 53. Film damping settings based on Veijola *et al.* 2005 paper (From: Veijola *et al.*, 2005).

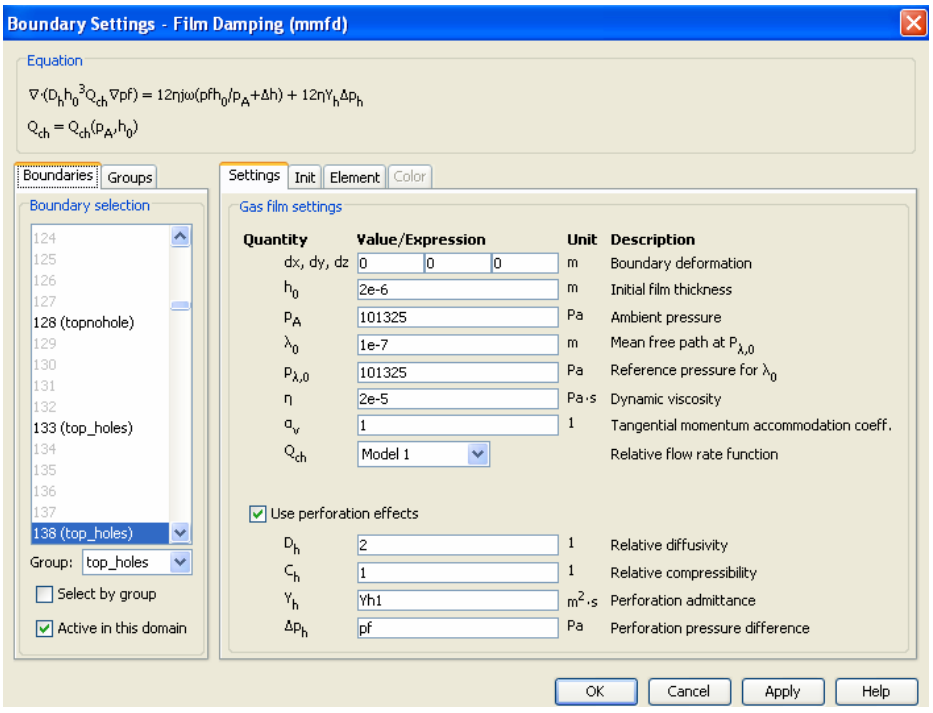

Figure 54. Film damping settings for the regions defined as holes.

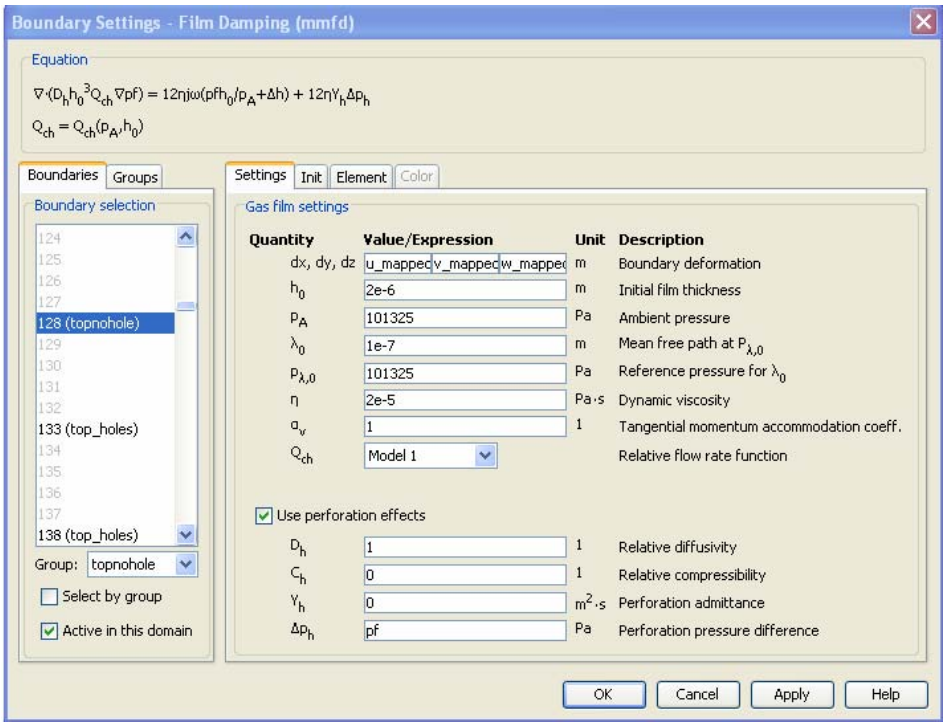

Figure 55. Film damping settings for the regions not defined as holes.

2. Device #19 Results

Figure 56 shows that device 19 is under damped as was calculated previously in Chapter IV. The simulation was to apply a force of one Pascal to the left wing (which is the upper half in the figure), and determine the damping pressure magnitude. Figure 56 shows that there is an average damping pressure less than 0.5 Pascals. Even though there are a few places with spots as high as 1.5 Pascals the average damping is less than 0.5 Pascals. Further research is needed to validate these findings and to ensure that the *COMSOL* simulation, using the modified Reynolds equation, is accurate. However, based on the frequency response curve damping calculations conducted in Chapter IV, which showed an under damped situation, the results of the simulation are in agreement that the device is under damped.

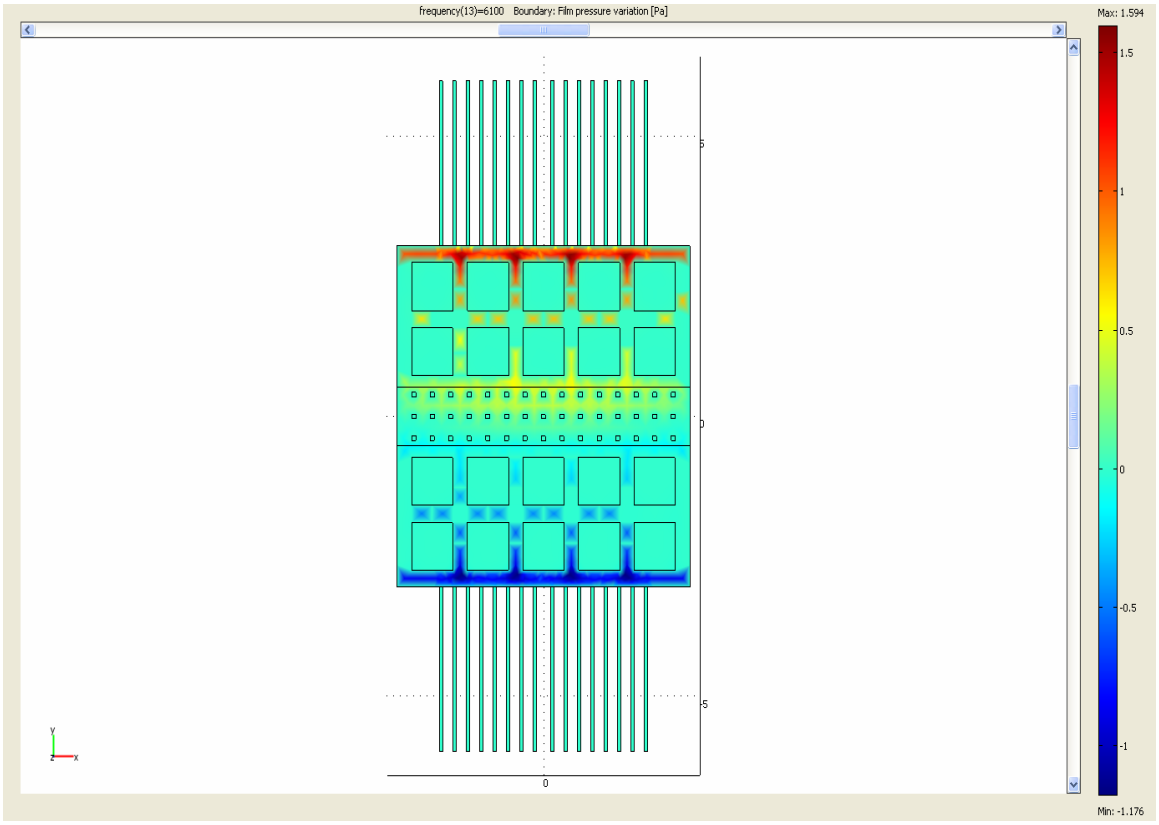

Figure 56. Device 19 damping pressure results for actuation at 6.1kHz for a one Pascal force.

THIS PAGE INTENTIONALLY LEFT BLANK

VI. CONCLUSION

It was shown that it is possible to design and fabricate a biomimetic MEMS based directional acoustic sensor that displays the expected rocking and bending modes of vibration, similar to those of the fly Ormia ochracea. Fabrication of the sensor, utilizing the PolyMUMPs process was also proven possible. However, the current designs evaluated produced amplitudes of vibrations one order of magnitude smaller than expected values. In which case, simulations agreed well with obtained results. Thorough simulation studies indicated that due to the longitudinal character of sound waves, the front side holes used for reducing damping greatly diminished the pressure difference across the plate surfaces. In which case, simulations agreed well with obtained results. Further efforts were performed to design a working model. Simulations showed that a solid plate would produce a larger displacement in the sound field. Simulations showed that a solid plate would produce a larger displacement in the sound field. However, damping becomes a large issue with a solid plate. Further modeling efforts showed encouraging results where by locating holes in the substrate (rather than in the vibrating plates) the damping can be controlled to desired levels. However, this direction leads to specialized processes – thus increasing costs. Nonetheless recent modeling efforts on Silicon-On-Insulator (SOI) MUMPs process, which allows for etching of the substrate, indicate potential for designing this biomimetic MEMS device on a standardized process. Further work is required to obtain an optimum design for this biomimetic MEMS sensor that can be fabricated on a standard process.

THIS PAGE INTENTIONALLY LEFT BLANK

VII. RECOMMENDATIONS FOR FUTURE WORK

A. INVESTIGATION OF SOIMUMPS PROCESS

In order to achieve the optimized performance of the sensor it is recommended that future research be focused on the SOIMUMPs process, focusing on solid plates. Damping control can be achieved via batch etching the damping holes in the substrate for minimal cost increase. Figure 57 shows a graphical idea of what the sensor should look like in 3D; the plate is approximately 10 micrometers thick, while the substrate is 400-500 micrometers thick. Figure 58 shows the same SOI device, but is a side view so that the etched holes are visible.

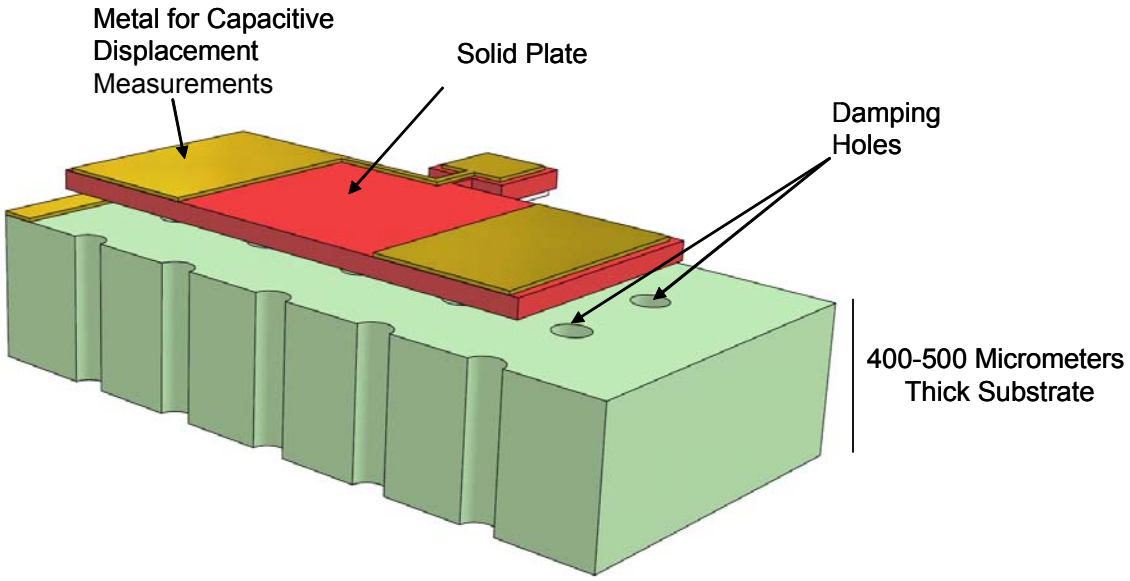

Figure 57. Recommend Sensor layout with perforated holes on the back plate to increase vibration amplitude and reduce squeezed film damping.

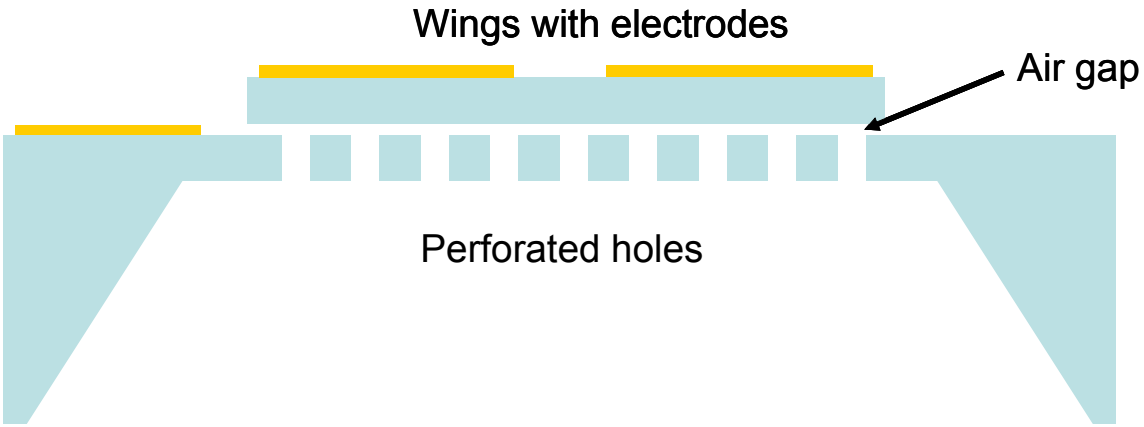

Figure 58. Recommend Sensor layout side view showing etched holes under wing structure. Again substrate is 400-500 micrometers thick, while the wings are only 10 micrometers thick, so this is not drawn to scale.

B. *COMSOL* SIMULATIONS OF THE SOIMUMPS PROCESS

Finally simulations should be done for how the air will escape through the etched holes in the substrate and the damping that is created from this air flow.

C. ADDITIONAL WORK

There is much room for future research related to this Thesis topic. Listed below are just a few examples of future research needed to perfect this biomimetic sensor, not related to the SOIMUMPs process. They are in no particular order.

a) Verify the *COMSOL* simulation, using the modified Reynolds equation, is accurate.

b) Working out the optimum settings for the M3110 Capacitance Measurement Chip and the placement of the boards components on the same chip as the sensor.

c) Determining power consumption and bearing resolution.

d) Verify operation in a noisy environment; measure signal to noise ratio. Determine the degradation in the bearing resolution in this noisy environment.

e) Working out placement of devices to measure in 2D, and then eventually in 3D.

f) Packaging issues for device to work underwater; keeping in mind the impedance differences between the water and the air in the package might affect the angle information.

g) Creating an array of perfected sensors.

THIS PAGE INTENTIONALLY LEFT BLANK

APPENDIX A – *MATLAB CODE SAMPLE FOR FLY ANIMATION*

```
% Script file:Fly_ear_animatedrev2.m
%
% Purpose: Program for calculating displacement of the two membranes
% Values are referenced from the 1995 Miles et al: Mechanically coupled
% ears.... paper.
%
%  The program does the following:
%  1. Calculates the membrane displacements left and right
%  2. Animates the results
%
%  Personnel who have worked on the program:
%   1) LT Tim Shivok
%   2) Jeff Catterlin (high school intern)
%   3) Professor Guest
%
% Record of revisions:
%    Date          Programmer      Class     Description of change
%    ====          ==========      =====     =====================
%  08/15/06       Timothy Shivok   Thesis    Original code
%  08/31/06       Prof. Guest                rev1-Modified code to add
%                                            animated results
%  09/05/06       Timothy Shivok   Thesis    rev2-Modified code to
%                                            solve for wt,wr,et, and er
%                                            vice use set results. Also
%                                            added the calculations for
%                                            both X and Y values vice
%                                            just one.
%
% 09/07/06        Prof. Guest                Added code to create avi
%                                            movie
%
%
clear all;
clc;
%
% Set the constants
m=2.88e-10; %kg --> effective mass of the organ
k1=.576; % N/m --> left membrane spring constant
k2=.576; % N/m --> right membrane spring constant
k3=5.18; % N/m --> coupling of membrane spring constant
c1=1.15e-5; %N s/m --> left membrane damping constant
c2=1.15e-5; %N s/m --> right membrane damping constant
c3=2.88e-5; %N s/m --> coupling of membrane damping constant
s=2.88e-7; %m^2 --> surface area????????
d=1.2e-3; %m --> distance between the force locations
%
% Calculate freq and damp ratio
%
wr=(k1/m)^.5; %calculates wr for any values of k vice setting wr=[44700
rad/sec --> (7120 Hz) first natural freq]
```

```
wt=((k1+2*k3)/m)^.5; %calculates wr for any values of k vice setting
wt=[195000 rad/sec --> (31000 Hz) second natural freq]
er=(c1)/(wr*m);%calculates er for any values of k vice setting er=[0.89
--> damping ratio of the first resonant mode]
et=(c1+2*c3)/(wt*m);%calculates et for any values of k vice setting
et=[1.24 --> damping ratio of the second resonant mode]
%
%
% Eventually want to allow user to easily change these
angle = 0;
% angle=30;%degrees --> angle of the incident sound wave
theta=(angle/180)*pi; %rad--> angle of the incident sound wave
w=2*pi*10000; %rad/sec --> 10000 Hz) Excitation frequency
P=1;%Pa --> Pressure Amplitude of the Sound Wave
%
%Calculate the values that do not change with time
tao=d*sin(theta)/344; %sec --> delay time due to angle
denomr=(wr^2-w^2)^2+(2*wr*er*w)^2;% inside sqrt of Denominator of the
Ar calc
denomt=(wt^2-w^2)^2+(2*wt*et*w)^2;% inside sqrt of Denominator of the
At calc
Ar=P*s/m*(sin(w*tao/2)/sqrt(denomr));%Amplitude of the response of the
rocking mode
At=P*s/m*(cos(w*tao/2)/sqrt(denomt));%Amplitude of the response of the
translating mode
Phir=-atan((2*wr*er*w)/(wr^2-w^2));% Phase constant rocking
Phit=-atan((2*wt*et*w)/(wt^2-w^2));% Phase constant translating
%
%
% Set our time steps
te=500e-6; %time end in seconds [This value is arbitrary and can be
changed]
t=0:2.5e-6:te;%time from 0 to time end
%
%Calculate the displacements Yl(t) and Yr(t) [Paper uses X, but to
%translate to the normal X and Y plane, I am calling it Y
for count = 1:1:(te/2.5e-6)+1
    Yl(count)=8e6*(At*sin(w.*t(count)+Phit) +
Ar*cos(w.*t(count)+Phir)); %left membrane displacement as a function of
time in micrometers
    Xl(count)=-(((.5)^2-Yl(count).^2).^.5);
    Yr(count)=8e6*(At*sin(w.*t(count)+Phit) -
Ar*cos(w.*t(count)+Phir)); %right membrane displacement as a function
of time in micrometers
    Xr(count)=((.5)^2-Yr(count).^2).^.5;
end;
    xarrow=.3*sin(theta);
    yarrow=.3*cos(theta)+.2;
% set up for avi movie:
scrsz = get(0,'ScreenSize'); %Gets dot length and width of screen
screensize=2  %Size can be adjusted by changing this variable.  The
larger the # the smaller the screen.  1 = entire screen.
fig = figure('Position',[1 1 scrsz(3)/screensize scrsz(4)/screensize]);
%sets the size of the figure to fill up most of the screen.
set(fig,'DoubleBuffer','on');
```

```
mov = avifile('flymovie.avi', 'COMPRESSION', 'none')

% draw the first position of the wings, represented as 3 points across:
%hwing=plot([Xl(1) 0 Xr(1)],[Yl(1) 0
Yr(1)],'LineWidth',4,'erasemode','xor')
hleft=plot([Xl(1) 0],[Yl(1) 0
],'LineWidth',8,'erasemode','xor','color','b')
hold on
hright=plot([ 0 Xr(1)],[ 0
Yr(1)],'LineWidth',8,'erasemode','xor','color','r')
hold on
harrow=plot([ 0 xarrow],[ 0.2
yarrow],'LineWidth',4,'erasemode','xor','color','k')

title ('Plot of Membrane Displacement for 10000kHz, 1
Pa','FontSize',14);
axis([-.6 .6 -.5 .5]);
xlabel('Length (mm)');
ylabel('Height/100 (nm)');
text(-.55, 0.4,['Direction of sound '],'FontSize',16)
text(0.4, 0.4,[' Deg '],'FontSize',16)
angletext = text(0.35,0.4,num2str(angle),'FontSize',16)

% Loop through wing movement for each wing:
for i=2:length(Xl)
 %change data given to handle hwing:
  % set(hwing,'xdata',[Xl(i) 0 Xr(i)],'ydata',[Yl(i) 0 Yr(i)]);
  set(hleft,'xdata',[Xl(i) 0],'ydata',[Yl(i) 0]);
  set(hright,'xdata',[0 Xr(i)],'ydata',[0 Yr(i)]);
  set(harrow,'xdata',[0 xarrow],'ydata',[.2 yarrow]);
  F = getframe(gca);
  mov = addframe(mov,F);
  drawnow

% Slow it down with a loop:
%     for slower = 1:50000
%         muchslower = slower * exp(2);
%    end
end


for angle = 30:30:60
% angle=30;%degrees --> angle of the incident sound wave
theta=(angle/180)*pi; %rad--> angle of the incident sound wave
w=2*pi*10000; %rad/sec --> 10000 Hz) Excitation frequency
P=1;%Pa --> Pressure Amplitude of the Sound Wave
%
%Calculate the values that do not change with time
tao=d*sin(theta)/344; %sec --> delay time due to angle
denomr=(wr^2-w^2)^2+(2*wr*er*w)^2;% inside sqrt of Denominator of the
Ar calc
denomt=(wt^2-w^2)^2+(2*wt*et*w)^2;% inside sqrt of Denominator of the
At calc
```

```
Ar=P*s/m*(sin(w*tao/2)/sqrt(denomr));%Amplitude of the response of the
rocking mode
At=P*s/m*(cos(w*tao/2)/sqrt(denomt));%Amplitude of the response of the
translating mode
Phir=-atan((2*wr*er*w)/(wr^2-w^2));% Phase constant rocking
Phit=-atan((2*wt*et*w)/(wt^2-w^2));% Phase constant translating
%
    xarrow=.3*sin(theta);
    yarrow=.3*cos(theta)+.2;
%
% Set our time steps
te=500e-6; %time end in seconds [This value is arbitrary and can be
changed]
t=0:2.5e-6:te;%time from 0 to time end
%
%Calculate the displacements Yl(t) and Yr(t) [Paper uses X, but to
%translate to the normal X and Y plane, I am calling it Y
for count = 1:1:(te/2.5e-6)+1
    Yl(count)=8e6*(At*sin(w.*t(count)+Phit) +
Ar*cos(w.*t(count)+Phir)); %left membrane displacement as a function of
time in micrometers
    Xl(count)=-((((.5)^2-Yl(count).^2).^.5);
    Yr(count)=8e6*(At*sin(w.*t(count)+Phit) -
Ar*cos(w.*t(count)+Phir)); %right membrane displacement as a function
of time in micrometers
    Xr(count)=((.5)^2-Yr(count).^2).^.5;
end;



    set(angletext,'string',num2str(angle))

% Loop through wing movement for each wing:
for i=2:length(Xl)
 %change data given to handle hwing:
% set(hwing,'xdata',[Xl(i) 0 Xr(i)],'ydata',[Yl(i) 0 Yr(i)]);
set(hleft,'xdata',[Xl(i) 0],'ydata',[Yl(i) 0]);
set(hright,'xdata',[0 Xr(i)],'ydata',[0 Yr(i)]);
set(harrow,'xdata',[0 xarrow],'ydata',[0.2 yarrow]);
F = getframe(gca);
 mov = addframe(mov,F);

 drawnow

  % Slow it down with a loop:
%     for slower = 1:50000
%         muchslower = slower * exp(2);
 %    end
end
end
mov = close(mov);
```

APPENDIX B – DR. KIM'S *ANSYS* CODE

```
Finish
/clear,nostart
/prep7

*DIM,A,array,100,3
*CREATE,ansuitmp
*VREAD,A(1,1),data1,m,,JIK,3,100
(3F10.4)
*END
/INPUT,ansuitmp

et,3,solid 45                !element for membrane
ET, 1,136,1 !     ! 4-node option, High Knudsen Number
ET, 2,138,1                  ! Circular hole option, High Knudsen Number
ET, 4,136,1 !0    ! 4-node option, High Knudsen Number
et,5,200,6

!geometric parameters
L=305 !690 ! !390          !um, length of mem
W=305  !um, half width of mem
L1=75 !37.5 !75 !um, length of torsion beam
W1=7    !um, half width of torsion beam
t=3.5     !um, thickness of Si
tau=0.5+0.75

parsav,1,para,txt               ! Save all parameter data
off1=5


!s_l1=1050                    ! Plate hole location to the length direction
!s_l2=600                           ! Plate hole location to the width direction

c_r=43 !60                    ! Hole radius
d_el=2 !+1                    ! Gap+alpha to adjust dmp/3
d_el2=2 !+1                         !gap2+alpha to adjust dmp/3
d_l=30
d_v=30
L2=L-(c_r+d_l-off1)        !um, length of mem for hole

hnum_l=3 !4                         !half hole number to lateral,x
hnum_v=3 !4                         !half hole number to vertical,y

s_l1=(2*c_r+d_l)*hnum_l !  % Plate hole location to the length direction
s_l2=(2*c_r+d_v)*hnum_v !

pamb=0.1                     ! ambient pressure (MPa)
visc=18.3e-12                ! viscosity kg/(um)(s)
pref=0.1                    ! Reference pressure (MPa)
mfp=64e-3                    ! mean free path (um)
Knud=mfp/d_el                ! Knudsen number
```

```
!!!!!!!!!!!!Grating
L_g=300 !200    !length of grating
W_g=7  !width of grating
W_d=7             !
W_h=W_g/2+W_d         !half width of hole
n_g=8   !half number of grating


mp,visc,1,visc              ! Dynamic viscosity gap
mp,visc,2,visc                      ! Dynamic viscosity holes
mp,visc,4,visc              ! Dynamic viscosity gap
mp,ex,3,130e3                       !modulus of Si
mp,nuxy,3,0.28                      !poissons ratio Si
mp,dens,3,2.32e-15                  !density of Si
mp,damp,5,7.182955*e-5          ! Material damping (from squeeze film results)


r,1,d_el,,,pamb                     ! Real constants - gap
rmore,pref,mfp

r,2,c_r,,,pamb                       ! Real constants - hole
rmore,pref,mfp

r,4,d_el2,,,pamb                            ! Real constants - gap
rmore,pref,mfp

!!!!!!!!!!!!BUILD MODEL!!!!!!
!create membrane
!block,0,L,-W,W,0,t
!block,0,-L,-W,W,0,t
!block,-W1,W1,W,W+L1,0,t
!block,-W1,W1,-W,-W-L1,0,t

!vsel,all
!vglue,all
!vplot

rectng,-L,L,-W,W
rectng,c_r+d_l,3*c_r+d_l,c_r,-c_r
agen,hnum_l-1,2,,,s_l1/hnum_l
rectng,-c_r-d_l,-3*c_r-d_l,c_r,-c_r
agen,hnum_l-1,hnum_l+1,,,-s_l1/hnum_l
agen,hnum_v,2,1+2*(hnum_l-1),,,s_l2/hnum_v
agen,hnum_v,2,1+2*(hnum_l-1),,,-s_l2/hnum_v
ASBA, 1, all

K,5001,L-L2,w,0
K,5002,L-L2,-w,0
K,5003,-L+L2,w,0
K,5004,-L+L2,-w,0
L,5001,5002,
L,5003,5004,

lnum=4*(2*hnum_l-2)*(2*hnum_v-1)+4   !line number
anum=1+(2*hnum_l-2)*(2*hnum_v-1)     !area number
```

```
LSEL,s,LINE,,lnum+1,lnum+2
ASBL,anum+1,all,,delete,delete
!ASBL,86,all,,delete,delete

rectng,-W1,W1,W,W+L1
rectng,-W1,W1,-W,-W-L1

!grating
*do,jj,1,n_g
rectng,L,L+L_g,W_h*(1+2*(jj-1))+W_g*(jj-1),W_h*(1+2*(jj-1))+W_g*jj
rectng,L,L+L_g,-W_h*(1+2*(jj-1))-W_g*(jj-1),-W_h*(1+2*(jj-1))-W_g*jj
rectng,-L,-L-L_g,W_h*(1+2*(jj-1))+W_g*(jj-1),W_h*(1+2*(jj-1))+W_g*jj
rectng,-L,-L-L_g,-W_h*(1+2*(jj-1))-W_g*(jj-1),-W_h*(1+2*(jj-1))-W_g*jj
*enddo

aglue,all

TYPE, 4
MAT, 4
esize,10
!smrtsize,1
AMESH, 39,40



TYPE, 1
MAT, 1
esize,20 !10
!smrtsize,1
!AMESH, 1,2,1
AMESH, 4,5,1
AMESH, 38


TYPE, 5
MAT, 5
smrtsize,10 !5
AMESH, 6,37

! Begin Hole generation
*do,j,1,(2*hnum_v-1)
*do,i,1,(hnum_l-1)
k=i+(j-1)*(hnum_l-1)
 nsel,all
 *GET, numb, node, , num, max       ! Create nodes for link elements

 N, numb+1,(i+0)*s_l1/hnum_l,-s_l2+j*s_l2/hnum_v,
 N, numb+2,(i+0)*s_l1/hnum_l,-s_l2+j*s_l2/hnum_v, t

 TYPE,2
 MAT, 2
 REAL,2
 NSEL, all
 E, numb+1, numb+2         ! Define 2-D link element
```

```
 ESEL, s, type,,1
 ESEL,a,type,,4
 NSLE,s,1

 local,11,0,(i+0)*s_l1/hnum_l,-s_l2+j*s_l2/hnum_v

 csys,11
 NSEL,r, loc, x, -c_r,c_r       ! Select all nodes on the hole circumference
 NSEL,r, loc, y, -c_r,c_r       ! Select all nodes on the hole circumference
 NSEL,a, node, ,numb+1

*GET, next, node, , num, min
 CP, k, pres, numb+1, next
 nsel,u,node, ,numb+1
 nsel,u,node, ,next
 CP, k, pres,all  !Coupled DOF set for constant pressure
 csys,0
*enddo
*enddo


*do,j,1,(2*hnum_v-1)
*do,i,1,(hnum_l-1)
kk=k+i+(j-1)*(hnum_l-1)
 nsel,all
 *GET, numb, node, , num, max       ! Create nodes for link elements

 N, numb+1,-(i+0)*s_l1/hnum_l,-s_l2+j*s_l2/hnum_v,
 N, numb+2,-(i+0)*s_l1/hnum_l,-s_l2+j*s_l2/hnum_v, t
 TYPE,2
 MAT, 2
 REAL,2
 NSEL, all
 E, numb+1, numb+2         ! Define 2-D link element
 ESEL, s, type,,1
 ESEL,a,type,,4
 NSLE,s,1

 local,11,0,-(i+0)*s_l1/hnum_l,-s_l2+j*s_l2/hnum_v
 csys,11
 NSEL,r, loc, x, -c_r,c_r       ! Select all nodes on the hole circumference
 NSEL,r, loc, y, -c_r,c_r       ! Select all nodes on the hole circumference
 NSEL,a, node, ,numb+1

*GET, next, node, , num, min
 CP, kk, pres, numb+1, next
 nsel,u,node, ,numb+1
 nsel,u,node, ,next
 CP, kk, pres,all             !Coupled DOF set for constant pressure
 csys,0
*enddo
*enddo

 ! End hole generation
```

```
esize,,2
type,3
mat,3
real,3
vext,all,,,,,t              ! Extrude structural domain

esize,,2 !1
type,3
mat,3
real,3
vext,208,,,,,tau            ! Extrude structural domain
!vext,1,,,,,tau             ! Extrude structural domain
!vext,43,,,,,tau            ! Extrude structural domain

nsel,s,loc,x,L
nsel,a,loc,x,-L
nsel,a,loc,y,-W-L1
nsel,a,loc,y,W+L1
nsel,r,loc,z,-1e-9,1e-9
d,all,pres,              ! Fix pressure at outer plate boundary
nsel,all

nsel,s,loc,y,W
nsel,a,loc,y,-W
nsel,u,loc,x,-W1,W1
nsel,r,loc,z,-1e-9,1e-9
d,all,pres,              ! Fix pressure at outer plate boundary
nsel,all

nsel,s,loc,x,W1
nsel,a,loc,x,-W1
nsel,u,loc,y,-W,W
nsel,r,loc,z,-1e-9,1e-9
d,all,pres,              ! Fix pressure at outer plate boundary
nsel,all

esel,s,type,,2
nsle,s,1
nsel,r,loc,z,t
d,all,pres,0          ! P=0 at top of plate
!dlist,all

esel,s,type,,1
esel,a,type,,4
nsle,s,1
!nsle,a,4
!nsle,s,all
nsel,u,cp,,1,2*(hnum_l-1)*(2*hnum_v-1)
cm,FLUN,node
allsel

!membrane boundary condtions
asel,s,loc,y,W+L1-0.01,W+L1+0.01        !select area parallel to x axis
asel,a,loc,y,-W-L1-0.01,-W-L1+0.01      !select area parallel to x axis
nsla,s,1
```

```
d,all,ux,0
d,all,uy,0
d,all,uz,0
allsel

finish

/solu
!antyp,harm                ! Full Harmonic analysis
!harfrq,4000

antype,modal                    ! Modal analysis
modopt,lanb,2                   ! Extract lowest two eigenmodes
eqslv,sparse
mxpand,2                            ! Expand lowest two eigenmodes
solve
fini

/post1
RMFLVEC          ! Extract eigenvectors
fini

/solu
fr1=1
fr2=60000
DMPEXT,1,1,d_damp,fr1,fr2,10
DMPEXT,2,2,d_damp,fr1,fr2,10
!DMPEXT,3,3,d_damp,fr1,fr2,10

/POST1
SET,LIST,999

/solu
abextract,1,2      ! Extract damping ratios and Rayleigh constants
finish
```

APPENDIX C – PROOF OF FW$\sqrt{2}$M

$$m\ddot{x} + b\dot{x} + kx = F_o \sin \omega t$$

$$\ddot{x} + \gamma \dot{x} + \omega_o{}^2 x = \frac{F_o}{m} \sin \omega t$$

$$\gamma = b/m \quad \omega_o{}^2 = k/m$$

$$x_o = \frac{F_o / m}{[(\omega_o{}^2 - \omega^2)^2 + (\gamma\omega)^2]^{\frac{1}{2}}}$$

$$x_o = \frac{F_o / (m\omega_o{}^2)}{[(1 - \omega^2 / \omega_o{}^2)^2 + (\gamma\, \omega / \omega_o{}^2)^2]^{\frac{1}{2}}}$$

$$\Omega = \omega / \omega_o \qquad \Gamma = \gamma / \omega_o$$

$$\Rightarrow x_o = \frac{F_o / (m\omega_o{}^2)}{[(1-\Omega^2)^2 + (\Gamma^2\Omega^2)^2]^{\frac{1}{2}}}$$

$$v_o = \omega x_o = \frac{\frac{F_o}{(m\omega_o)} \cdot \frac{\omega}{\omega_o} (= \Omega)}{[(1-\Omega^2)^2 + (\Gamma^2\Omega^2)^2]^{\frac{1}{2}}}$$

$$\Rightarrow v_o = \frac{F_o / (m\omega_o)}{[(\frac{1-\Omega^2}{\Omega})^2 + (\Gamma^2)^2]^{\frac{1}{2}}}$$

$$v_o(\max) = \frac{F_o / (m\omega_o)}{\Gamma} \Rightarrow \Omega = 1, \omega = \omega_o$$

$$\frac{v_o}{v_o(\max)} = \frac{\Gamma}{[\Gamma^2 + (\frac{1-\Omega^2}{\Omega})^2]^{\frac{1}{2}}}$$

$$\Rightarrow \frac{v_o}{v_o(\max)} = \frac{1}{[1 + (\frac{1-\Omega^2}{\Gamma\Omega})^2]^{\frac{1}{2}}}$$

So if $\frac{v_o}{v_o(\max)} = \frac{1}{\sqrt{2}}$ then:

$$\frac{v_o}{v_o(\max)} = \frac{1}{[1+(\frac{1-\Omega^2}{\Gamma\Omega})^2]^{\frac{1}{2}}} = \frac{1}{\sqrt{2}}$$

So denominator must equal 2, thus $(\frac{1-\Omega^2}{\Gamma\Omega})^2 = 1$. Therefore, take square root of both sides: $(1-\Omega^2) = \pm\Gamma\Omega$

$$\Omega^2 \pm \Gamma\Omega - 1 = 0$$

$$\Omega = \frac{\overset{-}{+}\Gamma \pm \sqrt{\Gamma^2+4}}{2}$$

$$\Omega_1 = -\frac{\Gamma}{2} + \frac{\sqrt{\Gamma^2+4}}{2}$$

$$\Omega_2 = +\frac{\Gamma}{2} + \frac{\sqrt{\Gamma^2+4}}{2}$$

Negative gamma is not possible

$$\Omega_2 - \Omega_1 = \Gamma$$

$$\frac{\Delta\omega}{\omega_o} = \frac{\gamma}{\omega_o} \Rightarrow FW\sqrt{2}M = \gamma = 2\beta$$

LIST OF REFERENCES

Christe, K. (2003). *Neuroethology: Fly Hearing*. Retrieved August 30, 2007, from http://nelson.beckman.uiuc.edu/courses/neuroethol/models/fly_hearing/fly_hearing.html

COMSOL, (Version 3.3a), (2007). [Computer Software]. www.comsol.com.

COMSOL, (2006). *MEMS Module User's Guide. COMSOL.*

Cui, W. (2004). "Analysis, Desgin, and Fabrication of a Novel Silicon Microphone," Ph.D. Thesis, SUNY at Binghampton.

Irvine-Sensors, (2004). "MS3110BDPC Universal Capacitive Readout Eval Board," Retrieved August 30, 2007, from http://www.irvine-sensors.com/Chips&Modules.html.

Karunasiri, G., Sinibaldi, J., Kim, B. (2005). "NSF-MASINT Proposal Paper," 2-14.

Kim, B., Schmittdiel, M., Degertekin, F.L., and Kurfess, T.R. (2005). "Actively controlled diffraction grating interferometer MEMS devices," *Proceedings of SPIE*, 5721, 151-158.

Kinsler, L.E., Frey, A.R., Coppens, A.B., and Sanders, J.V. (2000). *Fundamentals of Acoustics (Fourth Edition)*. New York: John Wiley and Sons. 15-17.

Koester, D., Cowen, A., Mahadeven, R., Stonefield, M., and Hardy, B. (2003). *PolyMUMPS Design Handbook* (Revision 10). MEMSCAP. Retrieved August 30, 2007, from http://amnl.mie.utoronto.ca/content/links/polymumps.dr.v10.pdf.

MEMSCAP, (2003). *PolyMUMPS.* Retrieved August 30, 2007, from http://www.memsrus.com/nc-mumps.poly.html.

MEMSNET, (2007). *What is MEMS Technology?* Retrieved August 30, 2007, from http://www.memsnet.org/mems/what-is.html.

Miles, R.N., Robert, D., Hoy, R.R. (1995). "Mechanically coupled ears for directional hearing in the parasitoid fly *Ormia ochracea,*" J. of Acoustics Soc. Ame, 98, No 6, 3059-3070.

Rao, S.S. (2003). *Mechanical Vibrations (Fourth Edition).* New Jersey: Pearson Education, Inc. 383-399.

Robert, D., Read, M.P., and Hoy, R.R. (1994). “The tympanal hearing organ of the parasitoid fly *Ormia ochracea* (Diptera, Tachinidae, Ormiini)," Cell Tissue Res., 275, 63-78.

Robert, D., Edgecomb, R.S., Read, M.P., and Hoy, R.R. (1996). “Tympanal hearing in tachinid flies (Diptera, Tachinidae, Ormiini): the comparative morphology of innovation." Cell Tissue Res., 284, 435-448.

Taylor, J.R., (2005). *Classical Mechanics.* California: University Science Books. 187-192 & 417-430.

Veijola, T., and Raback, P. (2005). “A Method for Solving Arbitrary MEMS Perforation Problems with Rare Gas Effects,” NSTI-Nanotech 2005, www.nsti.org, ISBN 0-9767985-2-2, 3, 561-564. Retrieved September 1, 2007, from http://www.aplac.hut.fi/publications/msm-2005-1/msm2005-final-cd.pdf.

Yoo, K., Gibbons, C., Su, Q.T., Miles, R.N., and Tien, N.C. (2002). “Fabrication of biomimetic 3D structure diaphragms,” *Sensors and Actuators A*, 97-98, 448-456. Retrieved September 7, 2007, from http://www.sciencedirect.com/science/article/B6THG-44VG3P9-D/2/1628ef3517f3fbbab7dd63d41e4b9902.

INITIAL DISTRIBUTION LIST

1. Defense Technical Information Center
   Ft. Belvoir, Virginia

2. Dudley Knox Library
   Naval Postgraduate School
   Monterey, California

3. Professor Karunasiri, Gamani
   Department of Physics
   Naval Postgraduate School
   Monterey, California

4. Professor Sinibaldi, Jose
   Department of Mechanical and Astronautical Engineering
   Naval Postgraduate School
   Monterey, California

5. Dr. Waters, Richard
   Space and Naval Warfare System Center
   San Diego, California

6. Dr. Dunec, John
   COMSOL, Inc.
   Palo Alto, California

7. CDR Denise Kruse
   Department of Undersea Warfare
   Naval Postgraduate School
   Monterey, California

8. Professor Daphne Kapolka
   Department of Physics
   Naval Postgraduate School
   Monterey, California

9. Professor James Luscombe
   Department of Physics
   Naval Postgraduate School
   Monterey, California

10. Professor Donald Brutzman
Department of Undersea Warfare
Naval Postgraduate School
Monterey, California

11. Raymond G. Jones, RADM, USN (Ret.)
Department of Undersea Warfare
Naval Postgraduate School
Monterey, California

12. Jeffrey DeNatale
Manager, MEMS Department
Teledyne Scientific & Imaging, LLC
Thousand Oaks, California